University of Iowa
Iowa Research Online

Theses and Dissertations

2010

Lepton pair production in high energy μa scattering: cross sections, energy loss, and applications to underground lepton production

Alexander Palen Bulmahn
University of Iowa

Copyright 2010 Alexander Palen Bulmahn

This dissertation is available at Iowa Research Online: http://ir.uiowa.edu/etd/472

Recommended Citation
Bulmahn, Alexander Palen. "Lepton pair production in high energy μa scattering: cross sections, energy loss, and applications to underground lepton production." dissertation, University of Iowa, 2010.
http://ir.uiowa.edu/etd/472.

Follow this and additional works at: http://ir.uiowa.edu/etd

Part of the Physics Commons

LEPTON PAIR PRODUCTION IN HIGH ENERGY μA SCATTERING: CROSS SECTIONS, ENERGY LOSS, AND APPLICATIONS TO UNDERGROUND LEPTON PRODUCTION

by

Alexander Palen Bulmahn

An Abstract

Of a thesis submitted in partial fulfillment of the
requirements for the Doctor of Philosophy
degree in Physics in the
Graduate College of The
University of Iowa

May 2010

Thesis Supervisor: Professor Mary Hall Reno

ABSTRACT

I reevaluate the total cross section and energy loss parameter β for lepton pair production from interactions of high energy muons with atomic targets. Using a detailed structure function analysis, this evaluation is valid for both elastic and inelastic scattering and includes the entire range of allowed momentum transfers. The formalism presented here is applied to both e^+e^- and $\tau^+\tau^-$ pair production. This approach to the calculation of the cross section allows for a numerical evaluation of the energy distribution of the differential cross section. Using this numerical evaluation, and parameterizations for the atmospheric muon flux, I calculate the differential flux of high energy electrons and taus produced underground from incident muons, considering both conventional and prompt atmospheric muon fluxes. An approximate form for the differential charged current neutrino cross section is presented and used to calculate the differential flux of electrons and taus produced from incident neutrinos to compare to the production by incident muons. I also calculate the underground flux of photons produced via muon bremsstrahlung and discuss the electromagnetic background from these events. The relevance of high energy lepton production for underground Cherenkov detectors is discussed.

Abstract Approved: _____
Thesis Supervisor

_____
Title and Department

_____
Date

LEPTON PAIR PRODUCTION IN HIGH ENERGY μA SCATTERING: CROSS SECTIONS, ENERGY LOSS, AND APPLICATIONS TO UNDERGROUND LEPTON PRODUCTION

by

Alexander Palen Bulmahn

A thesis submitted in partial fulfillment of the
requirements for the Doctor of Philosophy
degree in Physics in the
Graduate College of The
University of Iowa

May 2010

Thesis Supervisor: Professor Mary Hall Reno

Graduate College
The University of Iowa
Iowa City, Iowa

CERTIFICATE OF APPROVAL

PH.D. THESIS

This is to certify that the Ph.D. thesis of

Alexander Palen Bulmahn

has been approved by the Examining Committee for the thesis requirement for the Doctor of Philosophy degree in Physics at the May 2010 graduation.

Thesis Committee: _____
Mary Hall Reno, Thesis Supervisor

_____
Vincent Rodgers

_____
Kenneth Gayley

_____
Wayne Polyzou

_____
Ina Sarcevic

_____
Tuong Ton-That

ABSTRACT

I reevaluate the total cross section and energy loss parameter β for lepton pair production from interactions of high energy muons with atomic targets. Using a detailed structure function analysis, this evaluation is valid for both elastic and inelastic scattering and includes the entire range of allowed momentum transfers. The formalism presented here is applied to both e^+e^- and $\tau^+\tau^-$ pair production. This approach to the calculation of the cross section allows for a numerical evaluation of the energy distribution of the differential cross section. Using this numerical evaluation, and parameterizations for the atmospheric muon flux, I calculate the differential flux of high energy electrons and taus produced underground from incident muons, considering both conventional and prompt atmospheric muon fluxes. An approximate form for the differential charged current neutrino cross section is presented and used to calculate the differential flux of electrons and taus produced from incident neutrinos to compare to the production by incident muons. I also calculate the underground flux of photons produced via muon bremsstrahlung and discuss the electromagnetic background from these events. The relevance of high energy lepton production for underground Cherenkov detectors is discussed.

TABLE OF CONTENTS

LIST OF TABLES v

LIST OF FIGURES vi

CHAPTER

1 INTRODUCTION 1

1.1 Atmospheric Muons as Signal and Background 1
1.2 Muon Energy Loss 2
1.3 New Results 4

2 NOTATION AND FORMALISM 8

2.1 Differential Cross Section 8
2.2 Structure Functions 12
2.2.1 Elastic Nucleon Scattering 13
2.2.2 Coherent Scattering 14
2.2.3 Incoherent Scattering 17
2.2.4 Inelastic Scattering 19

3 CROSS SECTIONS, ENERGY LOSS, AND DIFFERENTIAL CROSS SECTION 22

3.1 Cross Sections 22
3.1.1 Nucleon Scattering 22
3.1.2 Higher Z Targets 23
3.2 Energy Loss 26
3.3 Differential Cross Section 30
3.3.1 Direct e^+e^- Pair Production 30
3.3.2 Direct $\tau^+\tau^-$ Pair Production 33
3.3.3 Neutrino Charged Current Interactions 35

4 ATMOSPHERIC LEPTON FLUXES 40

4.1 Surface Fluxes 40
4.1.1 Atmospheric Muon Flux 40
4.1.2 Atmospheric Neutrino Fluxes 42
4.2 Depth Corrections 45

5 UNDERGROUND LEPTON PRODUCTION 49

5.1 Event Geometries 49
5.2 Underground Electron Production 49
5.2.1 Electron Production in IceCube 51

5.3 Underground Tau Production 57
5.3.1 PeV Taus in IceCube 59
5.3.2 Tau Production for HAWC 62

6 DISCUSSION 65

APPENDIX

A CHANGE OF VARIABLES AND LIMITS OF INTEGRATION . . 72

B MATRIX CONTRACTIONS 75

BIBLIOGRAPHY 78

LIST OF TABLES

2.1 The central values of the fit of Kelly [45] for electromagnetic form factors of the proton. 14

LIST OF FIGURES

2.1 Pair production diagrams for μA scattering. The Bethe-Heitler diagrams (I) give the dominant contributions. Pair production from a photon radiating from the incoming or outgoing muon and from the atomic target or final hadronic state are shown in II and III respectively. The diagrams were produced using Jaxodraw [40]. 9

3.1 Elastic and inelastic contributions to the cross section for e^+e^- pair production in μp scattering as a function of initial muon energy. . . 23

3.2 Elastic and inelastic contributions to the cross section for $\tau^+\tau^-$ pair production in μp scattering as a function of initial muon energy. . . 24

3.3 Contributions to the total cross section for (a) $\mu A \to \mu e^+e^- X$ and (b) $\mu A \to \mu\tau^+\tau^- X$ for standard rock ($Z = 11$, $A = 22$) targets from coherent, incoherent, and inelastic scattering. 25

3.4 Cross section divided by atomic number A for $\mu A \to \mu e^+e^- X$ as a function of initial muon energy E_μ. Shown are proton ($A = 1$), hydrogen ($A = 1$), ice ($A = 14.3$), standard rock ($A = 22$), and iron ($A = 55.847$) targets. 27

3.5 Elastic and inelastic contributions to the energy loss parameter β_{pair} for e^+e^- pair production in μp scattering as a function of initial muon energy E_μ. 28

3.6 Elastic and inelastic contributions to the energy loss parameter β_{pair} for $\tau^+\tau^-$ pair production in μp scattering as a function of initial muon energy E_μ. 29

3.7 Energy loss parameter β_{pair} for proton, hydrogen ($A = 1, Z = 1$), ice ($A = 14.3, Z = 7.23$), rock ($A = 22, Z = 11$), and iron ($A = 55.847, Z = 26$) targets as a function of initial muon energy 30

3.8 Energy loss parameter β_{pair} for $\tau^+\tau^-$pair production as a function of initial muon energy for standard rock, $A = 22$ 31

3.9 Differential cross section as a function of electron energy for $\mu A \to \mu e^+e^- X$ for fixed muon energies of 10^3, 10^6, and 10^9 GeV. Here $A = 14.3$ and $Z = 7.23$ for ice. The solid lines show our numerical result and the dashed lines show the approximation of Tannenbaum [22] using $v = (E_\mu - E'_\mu)/E_\mu \simeq 2E_e/(E_\mu - E_e/2)$. 34

3.10 Contributions to the differential cross section as a function of tau energy for $\mu A \to \mu\tau^+\tau^- X$ for fixed muon energy, $E_\mu = 10^6$ GeV. Here $A = 22$ and $Z = 11$ is used for standard rock. Indicated are the contributions from coherent scattering with the nucleus (coh), inelastic scattering (DIS), and scattering with individual nucleons (incoh-N) and electrons (incoh-e) in the target. 35

3.11 Differential neutrino-nucleon cross section defined by Eq. 3.9 with parameters from Eqs. (3.10-3.11). The solid lines represent numerical results using the CTEQ6 parton distribution functions [54] and the dashed lines are our approximate analytic formula. Fig. (a) is the differential cross section for $E_\nu \leq 3.5 \times 10^4$ GeV with the fit parameters defined in Eq. (3.10). The curves represent $E_\nu = 50, 100, 500, 1000, 5000, 10^4$ GeV from bottom to top. Fig. (b) is the differential cross section with parameters defined in Eq. (3.11). The curves represent incident neutrino energies $E_\nu = 10^5, 10^6, 10^8, 10^{10}, 10^{12}$ GeV from bottom to top. 39

3.12 Differential antineutrino-nucleon cross section defined by Eq. (3.9). The solid lines represent numerical results using the CTEQ6 parton distribution functions [54] and the dashed lines are the results of our approximate analytic formula. Fig. (a) is the differential cross section for $E_{\bar{\nu}} < 10^6$ GeV with the fit parameters defined in Eq. (3.12). The curves represent incident antineutrino energies of $E_{\bar{\nu}} = 100, 10^3, 10^4, 10^5$ GeV from bottom to top. Fig. (b) is the differential cross section with parameters defined in Eq. (3.11). The curves represent incident antineutrino energies $E_{\bar{\nu}} = 10^6, 10^8, 10^{10}, 10^{12}$ GeV from bottom to top. 40

4.1 Contributions to the atmospheric muon flux at sea level in the vertical direction. The solid curve represents the conventional muon flux given by Eq. (4.1). The dashed curve represents the prompt muon flux calculated from perterbative QCD given by Eq. (4.4) while the dot-dashed curve represents the prompt flux given in Eq. (4.5) calculated using a dipole model of the $c\bar{c}$ cross section. 44

4.2 Contributions to the atmospheric muon flux at a depth of 1.5 km in ice, $A = 14.3$. The solid curve represents the conventional muon flux given in Eq. (4.1). The dashed curve represents the prompt flux given by Eq. (4.4) while the dot-dashed curve represents the prompt flux given in Eq. (4.5). 48

5.1 The three types of event geometries considered here for underground lepton production by atmospheric muons. Figures (a) and (b) are the types of events being considered for IceCube. Figure (a) represents contained events, i.e., particle production and decay contained in the detector. Figure (b) represents particles produced outside of the detector with the particles then entering the detector vertically. Figure (c) is the type of events being considered for HAWC. Leptons are produced in and then exit the mountains surrounding the surface array. 51

5.2 The differential underground electron flux scaled by the square of the electron energy for electrons produced in ice between the vertical depths $1.5 \leq d \leq 2.5$ km. The solid curves represent the electron flux produced by incident vertical conventional fluxes of muons and neutrinos given by Eqs. (4.1 & 4.6). The dashed curves labeled prompt represent the contribution from an initial prompt flux given by Eq. (4.4) while the dot-dash curve is the contribution from the prompt flux given in Eq. (4.5). The dashed curve following the conventional $\mu \rightarrow e$ curve was calculated using the Tannenbaum approximation to $d\sigma_{pair}/dE_e$. 54

5.3 The differential underground electron and photon fluxes scaled by the square of the electron or photon energy for particles produced in ice ($A = 14.3$) between the vertical depths $1.5 \leq d \leq 2.5$ km. The solid curves represent the electron flux produced by incident vertical conventional (Eq. (4.1)) and prompt (Eq. (4.5)) atmospheric muons. The dashed curves show the conventional and prompt $\mu \rightarrow \gamma$ contribution. 56

5.4 Energy distributions for the differential bremsstrahlung cross section for the process $\mu A \rightarrow \mu\gamma X$ and the differential electron-positron pair production cross section. The solid curve represents pair production and the dashed curve muon bremsstrahlung. Both of the distributions have been calculated for fixed muon energy $E_\mu = 10^6$ GeV in ice, $A = 14.3$. 57

5.5 The differential flux of electrons and photons scaled by the square of the electron or photon energy calculated using the restriction $v_{e,\gamma}^{max} = 0.01$ ($E_\mu^{min} \approx 100 E_{e,\gamma}$). Shown in the plot are the differential flux of electrons and photons produced from both conventional (Eq. (4.1)) and prompt (Eq. (4.5)) incident atmospheric muons. 58

5.6 Differential tau flux scaled by the square of the final tau energy entering the detector at a depth of 1.5 km in ice. The lower solid line corresponds to tau production from a vertical incident conventional muon flux given in Eq. (4.1). The dashed and dot-dashed curve represents the tau flux from a vertical incident prompt flux given in Eq. (4.4) and Eq. (4.5) respectively. The top solid curve is for the tau flux produced with an incident prompt tau neutrino flux given in Eq. (4.8). 62

5.7 Differential tau flux scaled by the square of the final tau energy emerging from 1 km water equivalent of rock. We use a zenith angle of 45° for our incident fluxes. The lower solid line corresponds to tau production from an incident conventional muon flux given in Eq. (4.1). The dashed and dot-dashed curve represents the tau flux produced from the incident prompt muon fluxes given in Eq. (4.4) and Eq. (4.5) respectively. The top solid curve represents the tau flux produced from the incident prompt tau neutrino flux given in Eq. (4.8). 65

CHAPTER 1
INTRODUCTION

1.1 Atmospheric Muons as Signal and Background

The study of atmospheric muons is relevant for many areas of high energy physics. Atmospheric muons are created in air showers that are produced by cosmic ray collisions in the atmosphere. When cosmic rays collide with air nuclei, secondary mesons are produced via $p + N_{air} \rightarrow \pi, K, D, \ldots + X$ [1, 2, 3, 4, 5, 6]. The decay of these secondary mesons produces muons [5, 6, 7, 8, 9, 10, 11]. Studying the energy distribution of the atmospheric muon flux provides information about hadronic cross sections [1] at energies which can reach well above those that can be obtained by current accelerator experiments. Information can also be gained about the primary cosmic ray flux and composition.

When considering the atmospheric muon flux, there are two different production mechanisms, commonly referred to as "conventional" and "prompt" production [1, 3, 4]. Conventional muons come from the decay of light mesons, namely pions and kaons [1]. Prompt muons come from the decay of heavier mesons. The main contribution to the prompt atmospheric muon flux comes from the decay of charmed mesons, mostly D mesons [1]. Because the cross section for light meson production is much higher than that for production of charmed mesons, the conventional atmospheric muon flux provides the dominant contribution to the total flux for low muon energies. At higher energies, the lifetime of light mesons becomes larger, allowing them to reach the surface of the earth before decaying [4]. This leads to an increased contribution from prompt production as muon energy grows. Studying the atmospheric muon flux at high energy provides the opportunity to study the onset of the prompt production in the atmosphere [3, 5, 11].

Atmospheric muons also play an important role in neutrino experiments [4, 10, 12]. The large flux of atmospheric muons has pushed neutrino experiments underground or under ice. Even at large depths there is still a large background from atmospheric muon signals. For instance, the ratio of downward going muons to muon neutrino induced muons is on the order of 10^6 even at depths larger than 1.5 km under ice. In addition to the muon background, there is also an atmospheric muon neutrino flux that is directly related to the production of atmospheric muons via the leptonic decay channels of mesons [3, 4]. Due to high production rate of atmospheric muon neutrinos at high energy, neutrino oscillations provide a background to searches for cosmic and atmospheric produced tau neutrino signals through $\nu_\mu \rightarrow \nu_\tau$ [3].

1.2 Muon Energy Loss

Muon energy loss is an important ingredient in the detection of muons. Atmospheric muons are detected by underground and underwater detectors [10, 12, 13, 14, 15]. These experiments measure the atmospheric muon flux as a function of energy and zenith angle. As high energy muons travel through matter, they lose energy through ionization and electromagnetic interactions. One of the ways to characterize the atmospheric muon flux is through the energy loss relationship given by

$$-\langle \frac{dE}{dX} \rangle = \alpha + \sum_{i=1}^{3} \beta_i E \ . \tag{1.1}$$

Here, E represents the energy of the muon, X is the column depth, α represents the energy loss through ionization, and β is the electromagnetic energy loss parameter. The subscript i that runs from one to three represents the three electromagnetic interactions that contribute to muon energy loss: lepton pair production, bremsstrahlung, and photonuclear interactions.

There is a long history of calculating the electromagnetic energy loss of muons in transit [16, 17, 18, 19, 20, 21, 22, 23]. There have been extensive studies of the cross section for lepton pair production from a fast muon interacting with nuclear targets [16, 17, 18, 24, 25, 26, 27, 28, 29, 30, 31, 32, 33, 34]. Most of these calculations have been restricted to the approximation of a static target with low momentum transfers to that target. To account for the nuclear nature of the targets, the formulas for the energy loss parameter β for electron-positron pair production have historically contained a $Z(Z+1)$ dependence to account for scattering contributions from the nucleus (Z^2) and atomic electrons (Z) [19, 20, 23]. For energy loss through photonuclear interactions, an in-depth study on the dependence of β to the momentum transfer of the radiated photon has been done to account for contributions from inelastic scattering. In Ref. [23] it was shown that at high muon energy, contributions from high momentum transfers can not be ignored. For the muon bremsstrahlung differential cross section, a similar calculation has been carried to include the effects from target excitation [35]. Calculations of muon energy loss through lepton pair production have typically been restricted to low lepton mass and low momentum transfers. Muon trident production, $\mu A \to \mu\mu^-\mu^+X$, has also been calculated for nucleon [27, 30, 32, 33] and atomic targets [31, 32, 34]. The focus of this thesis is muon production of lepton pairs, incorporating the full range of allowed momentum transfers.

Signals of muon production of lepton pairs in underground detectors are ubiquitous. For high muon energies, the dominant contribution to muon energy loss is through lepton pair production. Most of the energy loss is through electron-positron pair production with low energy transfers, however, there is the potential, through rare events, for the outgoing leptons to carry a large fraction of the initial muon energy. There is also the potential for creation of high energy $\tau^+\tau^-$ pairs. Because

atmospheric production of tau neutrinos is quite low, muon production of high energy taus may produce tau signals in underground detectors in an energy regime where few are expected. The observation of muon produced lepton pairs at high energy will help to characterize the atmospheric muon flux. High energy lepton pair production also provides an opportunity to test the predictions of quantum electrodynamics at high energy.

1.3 New Results

In this thesis, I present the general formulas for the calculation of the differential and total cross section and energy loss parameter β for lepton pair production from a fast muon interacting with an atomic target. Due to a detailed structure function analysis, these formulas are valid for a large range of momentum transfers to the target. In addition to electron-positron pair production, the formulas presented here are also applied to muon production of $\tau^+\tau^-$ pairs. I do not include the calculation of muon trident production due to the complications that come from having identical particles in the final state [30, 31, 32, 33, 34]. The results from this work have been published with Reno in Refs. [36, 37].

In Chapter 2, the formalism used to calculate the differential pair production cross section will be developed. Following the work presented in Ref. [27], target recoil will be included in the kinematics. In the calculation of the total cross section and energy loss parameter β_{pair}, contributions from coherent scattering with the nucleus, inelastic scattering, and scattering with individual atomic electrons and nucleons within the nucleus will be included. The structure functions for elastic scattering contributions are modeled by Tsai [26]. For inelastic contributions, the structure functions are parameterized using data from HERA [38]. In accounting for the different scattering processes through the structure functions, the different contributions to the total cross section can be calculated individually to understand

the relative importance of each process. The discussion of the parameterizations of the structure functions will begin by looking at nucleon targets and then will extend to include higher Z targets.

The results for the total cross section and energy loss parameter β_{pair} for both electron-positron and $\tau^+\tau^-$ pair production are presented in Chapter 3. For the total cross section, the separate contributions from coherent, inelastic, and incoherent scattering are shown as a function of muon energy for both e^+e^- and $\tau^+\tau^-$ production. The results for the energy loss parameter β_{pair} are compared to the commonly used results from Kokoulin and Petrukin [18]. For both the total cross section and energy loss parameter, results are given for nucleon as well as higher Z targets. A summary of these results is presented in Ref. [36].

One of the benefits of the formalism developed here for the calculation of the total cross section is that the energy distribution of the differential cross section for fixed muon energy can be calculated numerically. The results of this numerical evaluation of the differential cross section for e^+e^- and $\tau^+\tau^-$ pair production are presented in Sections 3.3.1 & 3.3.2 respectively. This numerical evaluation of the differential cross section is used to calculate the differential flux of electrons and taus that are produced in underground detectors from incident atmospheric muons. As was noted earlier, atmospheric muons provide large backgrounds in searches for neutrino signals. To compare the flux of electrons and taus produced by atmospheric muons with the flux of electrons and taus produced by atmospheric electron and tau neutrinos, an approximate form for the charged current differential cross section for neutrino nucleon scattering is presented in Section 3.3.3.

One of the ingredients needed for the calculation of underground lepton production from incident muons and neutrinos are the atmospheric muon and neutrino fluxes. A summary of parameterizations for atmospheric lepton fluxes is presented

in Chapter 4. These parameterizations include both conventional and prompt atmospheric fluxes. In Chapter 5, I will review the steps needed to go from an atmospheric muon or neutrino flux to an electron or tau flux. The formalism presented for the calculation of underground lepton production can be applied to many detector geometries.

For electron production we have focused our calculation on the large underground Cherenkov detector IceCube. IceCube is a cubic kilometer ice Cherenkov detector located in Antartica at a depth of $\sim$ 1.5 km [10, 13]. The results for our calculation of the differential flux of electrons produced from both conventional and prompt atmospheric muons are given in Section 5.2.1. For comparison, we have also calculated the flux of electrons produced from incident conventional and prompt atmospheric electron neutrinos and antineutrinos. It is important to note that in Cherenkov detectors it is very difficult to distinguish electromagnetic showers produced by electrons from those produced by photons. For this reason, we have also calculated the underground photon flux produced by high energy muon bremsstrahlung to show the electromagnetic background from this process.

In addition to underground electron production, we also explore the possibility of tau production in IceCube. To do this, we have calculated the flux of high energy taus produced from both incident muons and tau neutrinos entering the detector at a depth of 1.5 km. The results for tau production in IceCube are show in Section 5.3.1. In addition to IceCube, we also explore the possibility for tau production in the mountains surrounding the High Altitude Water Cherenkov (HAWC) surface array. The HAWC surface array is a Cherenkov detector located in Mexico that sits in a mountain saddle at an altitude of 4.1 km [39]. HAWC has the potential to see showers produced from the decay of taus that exit the surrounding mountains. The results for the flux of taus produced from incident muons and tau neutrinos

and antineutrinos exiting the rock of the mountains are given in Section 5.3.2. A summary of the results for underground production of high energy leptons can be found in Ref. [37]. In the final chapter, I summarize our results and discuss their relevance in a broader scope.

CHAPTER 2
NOTATION AND FORMALISM

2.1 Differential Cross Section

I begin my discussion of the differential cross section by looking at electron-positron pair production. The formulas are general and can be used for $\tau^-\tau^+$ pairs by converting $m_e \to m_\tau$. In the expression for the squared matrix element I will follow the notation used by Kel'ner [25]. I use the notation from Akhundov, Bardin, and Shumeiko [27], who included target recoil in their calculation of the pair production cross section, for the kinematics.

There are six diagrams that contribute to lepton pair production in the scattering of a muon with an atomic target. These contributing diagrams are shown in Figure 2.1. The dominant contribution comes from the Bethe-Heitler diagrams shown in Figure 2.1 (I) [17, 32, 33]. In the calculations that follow, I neglect the contributions from the radiative diagrams (Figure 2.1 (II) and (III)). This is a reasonable approximation due to the fact that the radiative diagrams only contribute on the order of 0.1% to the total cross section [17] in μA scattering.

For electron-positron pair production, a muon with four momentum k interacts with an atomic target of four momentum p. The outgoing muon, four momentum k_1, is accompanied by an electron and positron, momentum p_- and p_+ respectively, as well as a hadronic final state, $p_x = \sum_{i=\text{hadrons}} p_i$. It is useful to use the usual Lorentz invariant expressions for the four momentum squared of the incoming and outgoing muon, $k^2 = k_1^2 = m_\mu^2$, as well as for the electron and positron, $p_-^2 = p_+^2 = m_e^2$. For the hadronic states, $p^2 = M_t^2$ denotes the target mass squared and $p_x^2 = M_x^2$ denotes the final hadronic state invariant mass squared.

The squared hadronic matrix element $H^{\mu\nu}$ is written in terms of the hadronic current J^μ and can be expressed as a decomposition into the structure functions

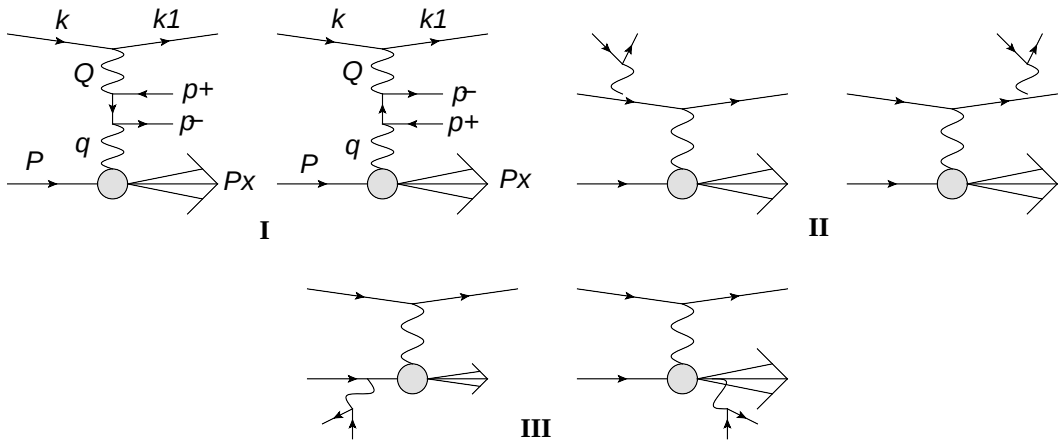

Figure 2.1: Pair production diagrams for μA scattering. The Bethe-Heitler diagrams (I) give the dominant contributions. Pair production from a photon radiating from the incoming or outgoing muon and from the atomic target or final hadronic state are shown in II and III respectively. The diagrams were produced using Jaxodraw [40].

F_1 and F_2. Using this method of decomposition, the tensor describing the hadronic vertex can be expressed as

$$e^2 H^{\mu\nu} = \frac{1}{2} \sum_{\text{spins, } X} \langle X|J^\mu|p\rangle \langle X|J^\nu|p\rangle^* \tag{2.1}$$

$$W^{\mu\nu} \equiv \frac{1}{4\pi M_t} \int H^{\mu\nu} (2\pi)^4 \delta^4 (p - q - \sum_{i=hadrons} p_i) \prod_i \frac{\mathrm{d}^3 p_i}{2E_i (2\pi)^3} \tag{2.2}$$

$$= (-g^{\mu\nu} + \frac{q^\alpha q^\beta}{q^2}) W_1 + (p^\mu - \frac{p \cdot q}{q^2} q^\mu)(p^\nu - \frac{p \cdot q}{q^2} q^\nu) \frac{W_2}{M_t^2} \tag{2.3}$$

$$= (-g^{\mu\nu} + \frac{q^\alpha q^\beta}{q^2}) \frac{F_1}{M_t} + (p^\mu - \frac{p \cdot q}{q^2} q^\mu)(p^\nu - \frac{p \cdot q}{q^2} q^\nu) \frac{1}{(p \cdot q) M_t} F_2 \ . \tag{2.4}$$

The expression for $W^{\mu\nu}$ is general and can be used to describe both elastic and inelastic scattering. It can also be used for a variety of nuclear targets. All of the target information is contained in the structure functions. The structure functions depend on the virtual photon four momentum squared, $q^2 = (p - p_x)^2$, and the Bjorken variable $x_{\text{Bj}} = q^2/2p \cdot q$ [41]. For elastic scattering $x_{\text{Bj}} = 1$, so the structure functions only depend on the value of the momentum transfer. Note that our choice for the sign of q is opposite that of the usual convention.

The spin averaged matrix element squared describing the muon contribution to the differential cross section is

$$A_{\alpha\beta} = \frac{1}{2}\mathrm{Tr}\Big[(\not{k}_1 + m_\mu)\gamma_\alpha(\not{k} + m_\mu)\gamma_\beta\Big]. \tag{2.5}$$

The change in momentum of the muon is defined by $Q \equiv k - k_1$. Following Ref. [25], the squared matrix element contribution from the virtual photon piece of the diagrams shown in Figure 2.1 (I), $\gamma^*(Q) + \gamma^*(q) \to e(p_-) + \bar{e}(p_+)$, can be written as

$$\begin{aligned} B^{\alpha\beta}_{\mu\nu} &= \mathrm{Tr}\Big[\left(\gamma_\alpha \frac{\not{q} - \not{p}_+ + m_e}{q^2 - 2qp_+}\gamma_\mu + \gamma_\mu \frac{\not{p}_- - \not{q} + m_e}{q^2 - 2qp_-}\gamma_\alpha\right)(\not{p}_+ - m_e) \\ &\times \left(\gamma_\beta \frac{\not{p}_- - \not{q} + m_e}{q^2 - 2qp_-}\gamma_\nu + \gamma_\nu \frac{\not{q} - \not{p}_+ + m_e}{q^2 - 2qp_+}\gamma_\beta\right)(\not{p}_- + m_e)\Big] \ . \end{aligned} \tag{2.6}$$

Again, this expression is general and can be used for $\tau^+\tau^-$ pair production with the substitution of $m_e \to m_\tau$.

Using these tensors, the differential cross section is expressed as

$$\mathrm{d}\sigma = \frac{4\pi M_t}{2\sqrt{\lambda_s}} A_{\alpha\beta} B^{\alpha\beta}_{\mu\nu} W^{\mu\nu} \frac{e^8}{q^4 Q^4} \delta^4(k + q - k_1 - p_+ - p_-)\mathrm{d}^4 q \tag{2.7}$$

$$\times \frac{\mathrm{d}^3 k_1}{2k_1^0 (2\pi)^3} \frac{\mathrm{d}^3 p_+}{2p_+^0 (2\pi)^3} \frac{\mathrm{d}^3 p_-}{2p_-^0 (2\pi)^3} \tag{2.8}$$

where $\lambda_s = (2p \cdot k)^2 - 4m_\mu^2 M_t^2$. To preform the phase-space integration, it is useful to rewrite all of the variables so that they are expressed in terms of Lorentz invariant quantities. These Lorentz invariants and the change of variables outlined in Appendix A [27], yield the differential cross section which can be written as

$$\mathrm{d}\sigma = \frac{1}{2\sqrt{\lambda_s}} A_{\alpha\beta} B^{\alpha\beta}_{\mu\nu} W^{\mu\nu} \frac{\alpha^4}{2\pi^4 t^2 Y^2} \mathrm{d}(PS) \ , \tag{2.9}$$

where $t = -q^2$ and $Y = -Q^2$, and the phase-space integration denoted by $\mathrm{d}(PS)$ is defined by

$$\mathrm{d}(PS) = \frac{\mathrm{d}\phi_1 \mathrm{d}S_x \, \mathrm{d}Y \mathrm{d}V^2 \, \mathrm{d}t \, \mathrm{d}M_x^2 \, \mathrm{d}\phi_q}{16\sqrt{\lambda_Y \lambda_s}} \mathrm{d}\Gamma_{\mathrm{pair}} \tag{2.10}$$

$$\mathrm{d}\Gamma_{\mathrm{pair}} = \delta^4(\kappa - p_+ - p_-) \frac{\mathrm{d}^3 p_+}{2p_+^0} \frac{\mathrm{d}^3 p_-}{2p_-^0} \tag{2.11}$$

$$= \frac{1}{8}\sqrt{1 - 4m_e^2/V^2} \ \mathrm{d}\cos\theta_e \, \mathrm{d}\phi_e \ . \tag{2.12}$$

To carry out the phase-space integration we have used the adaptive Monte-Carlo Fortran code VEGAS [42].

The evaluation of the matrix contractions can be simplified by evoking the gauge condition $B^{\alpha\beta}_{\mu\nu}q^\mu = 0$. Using this condition, the only surviving terms of the hadronic matrix element are

$$W^{\mu\nu} = -g^{\mu\nu}\frac{F_1}{M_t} + p^\mu p^\nu \frac{1}{(p\cdot q)M_t}F_2 \ . \tag{2.13}$$

Following Ref. [25], we define the quantity

$$\begin{aligned} f^{\alpha\beta} &= \int \frac{1}{q^4} B^{\alpha\beta}_{\mu\nu} W^{\mu\nu} \frac{d^3p_+}{2p^0_+}\frac{d^3p_-}{2p^0_-}\frac{d^4q}{2q^0}\delta^4(q+Q-p_+-p_-) \\ &= (g^{\alpha\beta} - \frac{Q^\alpha Q^\beta}{Q^2})f_A + \Big(p^\alpha - \frac{(p\cdot Q)Q^\alpha}{Q^2}\Big)\Big(p^\beta - \frac{(p\cdot Q)Q^\beta}{Q^2}\Big)f_B \end{aligned} \tag{2.14}$$

which depends only on the four-vectors p and Q. The terms f_A and f_B can be found using the gauge condition $f^{\alpha\beta}Q_\beta = 0$ as well as the contractions $g_{\alpha\beta}f^{\alpha\beta}$ and $p_\alpha p_\beta f^{\alpha\beta}$. Using Eq. (2.14) allows us to project out the surviving contractions of the matrix elements that can be expressed in terms of $g_{\alpha\beta}f^{\alpha\beta}$ and $p_\alpha p_\beta f^{\alpha\beta}$. These projections were calculated using the symbolic manipulation program FORM [43]. Because the expressions for the matrix contractions are quite long, I have not included them here but direct the reader to Appendix B.

It is important to note that because the integrand is proportional to dt/t^2 the evaluation of the cross section is dominated by values near the minimum t value. An approximate expression for t_{min} in elastic scattering is

$$t_{min} = \frac{4m_\mu^2 m_e^2}{E_\mu^2} \tag{2.15}$$

as discussed, for example, in Appendix A of Ref. [26]. For $\tau^+\tau^-$ pair production, one replaces $m_e^2 \to m_\tau^2$, so the minimum t is larger for $\tau^+\tau^-$ production than it is for e^+e^- production at the same energy. This has important ramifications for the relative importance of the different scattering contributions when comparing e^+e^-

pair production with $\tau^+\tau^-$ pair production.

2.2 Structure Functions

In calculating the pair production cross section for high energy μA scattering one needs to consider all of the contributions from the target. For nucleon targets, there are contributions from both elastic and inelastic scattering. For high Z targets, scattering can occur off of the coherent nucleus, bound electrons, individual nucleons contained in the nucleus, or individual quarks contained in the nucleons. It is instructive to look at the structure functions for the different processes separately.

For elastic scattering, the structure functions contain a delta function that enforces the relation $x_{\rm Bj} = 1$. To reduce the number of phase-space integrals it is useful to rewrite this delta function in terms of the final hadronic state invariant mass,

$$\delta(x_{\rm Bj} - 1) = t\delta(M_x^2 - M_t^2) \ . \tag{2.16}$$

In parameterizing the structure functions, the standard approach is to write them in terms of $\tau \equiv t/4M_t^2$, where M_t denotes the mass of the target. The structure functions for elastic scattering are normalized such that in the long wavelength limit, $t \to 0$, the virtual photon does not see any target structure, $F_1(0) = F_2(0) = 0$ [26]. I begin my discussion on structure functions with elastic scattering. I start with the simplest case of nucleon targets followed by a discussion of higher Z targets. For high Z targets, I first discuss coherent scattering with the nucleus followed with incoherent scattering off of nucleons and atomic electrons.

Finally, the structure functions for inelastic scattering is considered. For inelastic scattering, there is no delta function over $x_{\rm Bj}$, so there is an additional integral over the final state hadronic mass squared, M_x^2. The structure functions F_1

and F_2 for inelastic scattering are presented in terms of the inelastic proton structure functions. A nuclear shadowing function is multiplied to the nucleon structure functions to extend the calculation to atomic targets.

2.2.1 Elastic Nucleon Scattering

For nucleon targets, the target mass $M_t = M$, where M denotes the mass of the proton. The structure functions can be written in terms of the electric and magnetic form factors, G_E and G_M,

$$F_1^{\rm el} = \frac{t}{2} G_M^2 \; \delta(M_X^2 - M^2) \tag{2.17}$$

$$F_2^{\rm el} = \frac{t}{1+\tau}\Big(G_E^2 + \tau G_M^2\Big) \; \delta(M_X^2 - M^2) \; . \tag{2.18}$$

By treating nucleon targets as extended objects, the form factors can be written in the traditional dipole form [44]. For the proton

$$G(t) = (1 + t/0.71 \text{ GeV}^2)^{-2} \tag{2.19}$$

$$G_{Ep} = G(t) \tag{2.20}$$

$$G_{Mp} = \mu_p G(t) = 2.79 G(t) \tag{2.21}$$

where μ_p is the magnetic moment of the proton in units of nuclear magnetons. For the neutron, the form factors are

$$G_{En} = -\frac{\mu_n \tau}{1 + 5.6\tau} G(t) \tag{2.22}$$

$$G_{Mn} = \mu_n G(t) = -1.91 G(t) \; . \tag{2.23}$$

These form factors are consistent with the results of the Rosenbluth separation method, which analyzes at the angular distribution of the cross section as a function of t [44].

A more recent review of the nucleon elastic form factors, which studies the polarization transfer of polarized electrons to proton targets, appears in Refs. [44, 45]. Using this analysis, the electric and magnetic form factors for the proton can

Form factor	a_0	a_1	b_1	b_2	b_3
G'_{Ep}	1	-0.24	10.98	12.82	21.97
G'_{Mp}	1	0.12	10.97	18.86	6.55

Table 2.1: The central values of the fit of Kelly [45] for electromagnetic form factors of the proton.

be written as

$$G_{Ep} = G'_{Ep}(t) \tag{2.24}$$

$$G_{Mp} = \mu_p \, G'_{Mp}(t) \tag{2.25}$$

where generically,

$$G'(t) = \frac{\sum_{k=0}^{n} a_k \tau^k}{1 + \sum_{k=1}^{n+2} b_k \tau^k} \ . \tag{2.26}$$

The fit coefficients for the proton form factors are shown in Table 2.1. These fit coefficients are found by looking at the transverse and longitudinal contributions to the cross section to separate electric contributions from magnetic. This parametrization for the electric and magnetic form factors is valid over a larger range of t values and yields a better fit for the high t region than the form factors found using the Rosenbluth separation method [44]. However, since our calculation is centered around low t, these two parameterizations yield essentially the same results in the calculation of the total cross section and energy loss for pair production. For this reason, we will use the simpler form for the electric and magnetic form factors given in Eqs. (2.20-2.23) in the calculations that follow.

2.2.2 Coherent Scattering

For higher Z targets, the dominant contribution to the cross section, and also to the energy loss, comes from elastic, coherent scattering off of the nucleus. The

target nucleus carries a charge Z and a mass of $M_t = M_A = AM$ $(A \sim 2Z)$. This leads to a Z^2 dependence in the structure functions. The structure functions for nuclear targets can again be written in terms of the electric and magnetic form factors and have the same form as those for nucleon targets

$$F_1^{\rm coh} = \frac{t}{2} G_M^2 \delta(M_X^2 - M_A^2) \tag{2.27}$$

$$F_2^{\rm coh} = \frac{t}{1+\tau}\Big((F_n - F_e)^2 + \tau G_M^2\Big)\, \delta(M_X^2 - M_A^2)\ . \tag{2.28}$$

In the above equation, F_n is the electric nuclear form factor. In addition to carrying information about the nucleus, the effects of bound electrons are also included in the structure functions. For coherent scattering, bound electrons screen the coulomb field of the nucleus [26, 35, 46]. This screening effect is seen by the presence of the electric form factor for bound electrons, denoted by F_e in Eq. (2.28).

For nuclear targets, the electric components of the structure functions can be found using the non-relativistic electromagnetic current operator [35],

$$I_0(\mathbf{r}) = \sum_j \delta(\mathbf{r} - \mathbf{R_j}) - \sum_i \delta(\mathbf{r} - \mathbf{r_i})\ . \tag{2.29}$$

The atomic wave functions, which can be written as a product of wave functions for atomic electrons and protons,

$$\Psi(\mathbf{r_1}, \ldots, \mathbf{r_Z}; \mathbf{R_1}, \ldots, \mathbf{R_Z}) = \Psi^e(\mathbf{r_1}, \ldots, \mathbf{r_Z})\Psi^p(\mathbf{R_1}, \ldots, \mathbf{R_Z}), \tag{2.30}$$

are also needed to determine the charge density of the target [47]. For coherent scattering one needs only to consider the ground state wave functions of the atom [26, 35]. In Eq. (2.30), $\mathbf{r_n}$ denotes the coordinates of the atomic electrons and $\mathbf{R_n}$ are the coordinates of the protons in the nucleus. Using Eqs. (2.29-2.30), the electric contribution to the structure functions can be expressed as [35]

$$(F_n - F_e)^2 = \left| \int \langle 0|I_0(\mathbf{r})|0\rangle e^{i\mathbf{q}\cdot\mathbf{r}} d\mathbf{r} \right|^2\ . \tag{2.31}$$

Using this equation, the electronic and nuclear electric form factors are

$$F_n = \int \left(\sum_j e^{i\mathbf{q}\cdot\mathbf{R_j}} \right) |\psi_0^p(\mathbf{R_1} \ldots \mathbf{R_Z})|^2 d\mathbf{R_1} \ldots d\mathbf{R_Z} \tag{2.32}$$

$$F_e = \int \left(\sum_i e^{i\mathbf{q}\cdot\mathbf{r_i}} \right) |\psi_0^e(\mathbf{r_1} \ldots \mathbf{r_Z})|^2 d\mathbf{r_1} \ldots d\mathbf{r_Z} \ . \tag{2.33}$$

For hydrogen, the electronic wave function of the ground state is know exactly. Using the ground state wave function for hydrogen, an exact, analytic expression for the electronic form factor can be found [26] and is given by

$$F_e(t) = \frac{1}{(1 + \frac{a_0^2 t}{4})} \qquad (Z = 1) \ , \tag{2.34}$$

where $a_0 = 137/m_e$ defines the Bohr radius. The nuclear electric and magnetic form factors for the Hydrogen atom are the same as those for the proton found in Eqs. (2.20-2.23).

Because the wave functions for high Z (above helium) targets are very complicated, it is useful to find an approximate, analytical form for the form factors that can be used for calculation. For these high Z targets, the electric nuclear form factor can be approximated by [26, 46]

$$F_n = \frac{Z}{(1 + \frac{a^2 t}{12})^2} \tag{2.35}$$

$$a = (0.58 + 0.82 A^{1/3}) \times 5.07 \text{ GeV}^{-1} \ . \tag{2.36}$$

An expression for the electronic form factor associated with electron screening can be found in a similar way [26, 46, 48] yielding

$$F_e = \frac{Z}{(1 + b^2 t)} \tag{2.37}$$

$$b = \frac{184.15}{\sqrt{e}} Z^{-1/3} \frac{1}{m_e}. \tag{2.38}$$

Though the above equations are only approximate expressions, they yield results that agree to within $\sim 4\%$ with those found by using the more precise Thomas-Fermi form factors [48] and have a much simpler form useful for calculation.

For high Z targets, we ignore magnetic contributions to the coherent structure functions, $G_M \approx 0$. This is a reasonable approximation because the net magnetic moment for a multi-nucleon atom is small. In addition, for large atomic number A, the factor τ which always precedes G_M is also very small. For this reason, F_1 can be neglected.

2.2.3 Incoherent Scattering

Another component of elastic scattering is the incoherent scattering of the muon off of the individual nucleons inside of the nucleus. Again, the structure functions can be written in terms of the electric and magnetic form factors for the proton and neutron given in Eqs. (2.20-2.23). Because the scattering is off of nucleons, the target mass $M_t = M$, and the structure functions are given by

$$\begin{aligned} F_1^{\text{incoh,N}} &= C(t)\frac{t}{2}\Big(ZG_{Mp}^2 + (A-Z)G_{Mn}^2\Big)\delta(M_X^2 - M^2) && (2.39)\\ F_2^{\text{incoh,N}} &= C(t)\frac{t}{1+\tau}\Big(ZG_{Ep}^2 + (A-Z)G_{En}^2 && (2.40)\\ &+ \tau(ZG_{Mp}^2 + (A-Z)G_{Mn}^2)\Big)\ \delta(M_X^2 - M^2)\ . \end{aligned}$$

The function $C(t)$ in the above equations is the Pauli suppression factor defined by

$$C(t) = \begin{cases} \frac{3Q_P}{4P_F}\Big(1 - \frac{Q_P^2}{12P_F^2}\Big) & Q_P < 2P_F \\ 1 & \text{otherwise} \end{cases} \tag{2.41}$$

where $Q_P^2 = t^2/(4M^2)+t$ and $P_F = 0.25$ GeV [26]. The above expression is found by approximating the protons and neutrons within the nucleus as two non-interacting fermi gases [49].

A different parameterization for the structure function $F_2^{incoh,N}$,

$$F_2^{incoh,N} = Z\frac{t}{1+\tau}F_n^{incoh}\delta(M_X^2 - M^2)\ , \tag{2.42}$$

comes from including transitions to excited states in the nucleon part of Eq. (2.31),

$$F_n^{incoh} = \frac{1}{Z}\sum_{n\neq 0}\left|\int\sum_j \langle n|\delta(\mathbf{r}-\mathbf{R_j})|0\rangle e^{i\mathbf{q}\cdot\mathbf{r}}\right|^2\ , \tag{2.43}$$

and using the completeness condition for the set of states given by the relation [35]

$$\sum_n \Psi_n^{*p}(\mathbf{R_1},\ldots,\mathbf{R_Z})\Psi_n^p(\mathbf{R_1^{'}},\ldots,\mathbf{R_Z^{'}}) = \delta(\mathbf{R_1}-\mathbf{R_1^{'}})\ldots\delta(\mathbf{R_Z}-\mathbf{R_Z^{'}}) \ . \quad (2.44)$$

Using these relations, the form factor for incoherent nucleon scattering takes the form [26, 35, 46],

$$F_n^{incoh} = 1 - F_n^2 \quad (2.45)$$

where F_n is the nuclear electric form factor defined by Eq. (2.35). Though this structure function has a simple analytic form, it does not take into account magnetic effects. For the results presented in Chapter 3 for the total cross section and energy loss parameter β_{pair}, I use the structure functions defined in Eqs. (2.39-2.40) for the contributions from incoherent nucleon scattering.

Another contribution to incoherent scattering effects comes from atomic electrons. Atomic electrons, in addition to screening the Coulomb field of the nucleus, also provide targets for the incoming muon [28, 35]. For electron targets the target mass $M_t = m_e$. The structure functions for scattering off of individual bound electrons can be written

$$F_1^{\text{incoh,e}} = Z\frac{t}{2}\delta(M_x^2 - m_e^2) \quad (2.46)$$

$$F_2^{\text{incoh.e}} = Z\frac{t}{(1+\tau)}\left[F_e^{incoh} + \tau\right]\delta(M_x^2 - m_e^2) \ , \quad (2.47)$$

where F_e^{incoh} is the electric form factor associated with electron targets. In the above equations, the magnetic form factor has been set to one.

To find a form for the electric form factor, F_e^{incoh}, the same method is used as above for including transitions to excited states and the completeness condition given in Eqs. (2.43-2.44) using the electron wave functions [35]. This give the relation [26, 35]

$$F_e^{incoh} = 1 - ZF_e^2 + \frac{1}{Z}\int |\Psi_0^e(\mathbf{r_1},\ldots,\mathbf{r_Z})|^2 \sum_{i\neq j} e^{i\mathbf{q}\cdot(\mathbf{r_i}-\mathbf{r_j})} d\mathbf{r_1}\ldots d\mathbf{r_Z} \ , \quad (2.48)$$

with the expression for F_e given in Eq. (2.37).

For hydrogen, there is only one atomic electron, so the last term in Eq. (2.48) vanishes. The electric form factor for hydrogen reduces to [26]

$$F_e^{\mathrm{incoh,e}} = 1 - F_e(t)^2. \tag{2.49}$$

For higher Z atoms, the incoherent electric form factor for electron targets can be modeled by the approximate parameterization [26, 35, 46]

$$F_e^{incoh,e} = \frac{c^4 t^2}{(1+c^2 t)^2} \tag{2.50}$$

$$c = \frac{1194}{\sqrt{e}} Z^{-2/3} \frac{1}{m_e}. \tag{2.51}$$

The results found using this parameterization for the incoherent electron structure functions agree well with those found using the parameterization presented by Kel'ner [28]. For standard rock ($Z = 11$), the above expression for the structure function gives a result that is within 2% of that found using Eq. (46) of Ref. [28] for muon energy $E_\mu = 100$ GeV. For muon energy $E_\mu = 10^9$ GeV, the result found using Eq. (2.50) is $\sim 18\%$ larger than that found using Ref [28]. Neglecting contributions from additional diagrams that come from identical particle exchange in $\mu e^- \to \mu e^- e^- e^+$ is a reasonable approximation for the energies under consideration here [28]. For both incoherent nucleon and electron scattering, the structure functions are reduced by a factor of $1/Z$ relative to coherent scattering with the nucleus.

2.2.4 Inelastic Scattering

Inelastic scattering takes place when the momentum transfer to the target is above the threshold for pion production. At these momentum transfers, the virtual photon scatters off of individual quarks in the nucleons. Because of this, the

substructure of individual nucleons needs to be considered. For inelastic contributions to the cross section, we use the proton structure functions parametrized by Abramowicz, Levin, Levy and Maor (ALLM) [50], updated in Ref. [38]. The ALLM model is a phenomenological parameterization that is valid for a large range of $x_{\rm Bj}$ and t values, including the perturbative regime. Because inelastic scattering is probing the structure of individual nucleons, the target mass $M_t = M$. For a nucleus of charge Z and atomic number A, the structure functions for the nucleons are given by

$$\begin{aligned} F_2^N &= ZF_{2p}^{inel} + (A-Z)F_{2n}^{inel} && (2.52)\\ &= \Big(Z + (A-Z)P(x_{\rm Bj})\Big)F_{2p} && (2.53)\\ F_1^A &= F_2^N/(2x_{\rm Bj})\ . && (2.54) \end{aligned}$$

The parameterization for the proton structure function F_{2p}^{inel} in the ALLM model can be found in Ref. [38] and in the appendix of Ref. [23]. The ratio of the neutron structure function to the proton structure function, $F_{2n}^{inel}/F_{2p}^{inel}$, is taken into account using the polynomial $P(x_{\rm Bj})$ which is given by [51]

$$P(x_{\rm Bj}) = 1 - 1.85x_{\rm Bj} + 2.45x_{\rm Bj}^2 - 2.35x_{\rm Bj}^3 + x_{\rm Bj}^4\ . \qquad (2.55)$$

The structure function F_1^N is found using the Callan-Gross relation, namely $2x_{\rm Bj}F_1 = F_2$.

Because we are interested in muons scattering with atomic targets, nuclear shadowing effects also need to be included in the definitions of structure functions. For this reason we incorporate the shadowing function $a(A, x_{\rm Bj}, t) \simeq a(A, x_{\rm Bj})$ [52]

$$a(A, x_{\rm Bj}) = \begin{cases} A^{-0.1} & x_{\rm Bj} < 0.0014 \\ A^{0.069\log_{10} x_{\rm Bj} + 0.097} & 0.0014 < x_{\rm Bj} < 0.04 \\ 1 & 0.04 < x_{\rm Bj} \end{cases} \qquad (2.56)$$

into our calculation. Using Eq. (2.56), the structure functions for inelastic scattering

off of atomic targets are given by

$$F_2^A = a(A, x_{\rm Bj})\Big(Z + (A-Z)P(x_{\rm Bj})\Big)F_{2p} \tag{2.57}$$

$$F_1^A = a(A, x_{\rm Bj})F_2^N/(2x_{\rm Bj}) \ . \tag{2.58}$$

Since our calculation is dominated by low $x_{\rm Bj}$ values, the approximate scaling for inelastic scattering contributions is roughly $A^{0.9}$. The results for inelastic scattering of virtual photons with proton targets found using the parameterization for the proton structure functions in the ALLM model given in Ref. [38] are in good agreement with the results for real photons scattering off of proton targets as $t \to 0$.

CHAPTER 3
CROSS SECTIONS, ENERGY LOSS, AND DIFFERENTIAL CROSS SECTION

3.1 Cross Sections

3.1.1 Nucleon Scattering

The total cross section for lepton pair production from muons scattering with proton targets can be written as the sum of elastic and inelastic contributions

$$\sigma_{\mu p} = \sigma_{\mu p}^{el} + \sigma_{\mu p}^{inel} \ . \tag{3.1}$$

Figure 3.1 shows a plot of the elastic and inelastic contributions to the cross section as a function of initial muon energy for electron-positron pair production. As one can see from the plot, the elastic contribution to the total cross section is $\sim 5-6$ orders of magnitude larger than the inelastic contributions. This can be understood by looking at the approximate expression for the minimum t value, Eq. (2.15). The calculation for lepton pair production is dominated by values near t_{min}. Because $F_{2_p}^{inel}$ is small for $t \ll M^2$, the inelastic contribution to the total cross section is very small for electron-positron pair production.

For $\tau^+\tau^-$ pair production, t_{min} is much larger for a range of initial muon energies, so we expect to see a larger contribution from inelastic scattering. Figure 3.2 shows the elastic and inelastic contributions for μp scattering to produce tau pairs. Inelastic scattering contributes between 30% and 60% to the total cross section depending on intial muon energy for muon energies between 100 GeV $\leq E_\mu \leq 10^9$ GeV. Overall, the cross section for e^+e^- pair production is ~ 7 orders of magnitude larger than that for $\tau^+\tau^-$ pair production in μp scattering.

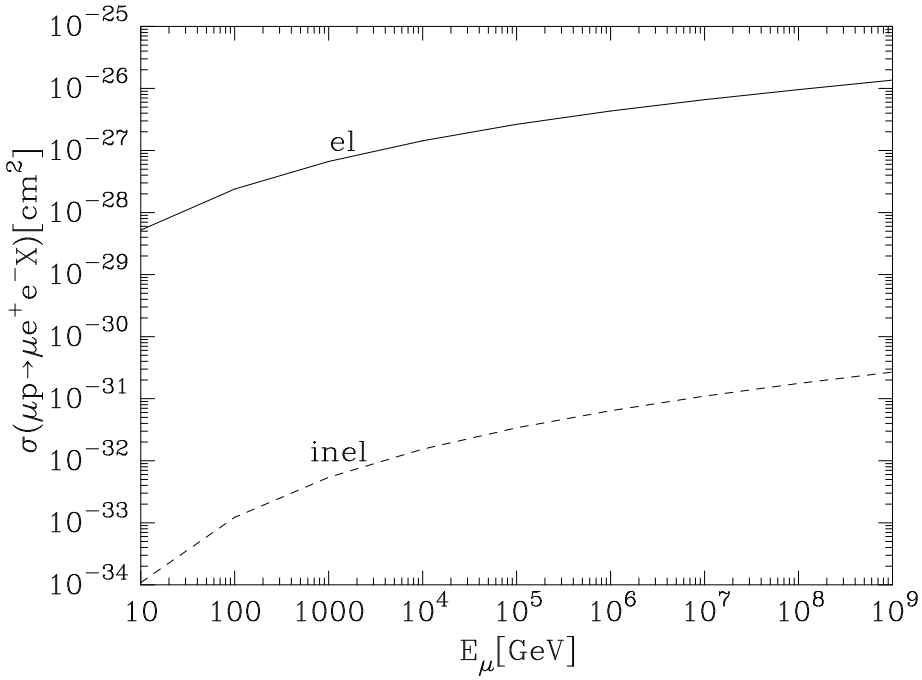

Figure 3.1: Elastic and inelastic contributions to the cross section for e^+e^- pair production in μp scattering as a function of initial muon energy.

3.1.2 Higher Z Targets

For higher Z targets, the total cross section can be written as the sum of contributions from coherent, incoherent, and inelastic scattering,

$$\sigma^{total} = \sigma^{coh} + \sigma^{incoh,N} + \sigma^{incoh,e} + \sigma^{inel} \ . \tag{3.2}$$

For both e^+e^- and $\tau^+\tau^-$ pair production, elastic coherent scattering with the nucleus, which goes like Z^2, gives the dominant contribution to the cross section at high initial muon energies ($E_\mu > 10^3$ GeV). For e^+e^- pair production, incoherent electron scattering, which is proportional to Z, contributes $\sim$ 10% to the total cross section for the muon energies considered here. The contribution to the total cross section from incoherent nucleon and inelastic scattering are not significant. A plot of the different scattering contributions to the total cross section for e^+e^- pair production in standard rock ($A = 22$) is shown in Figure 3.3 (a).

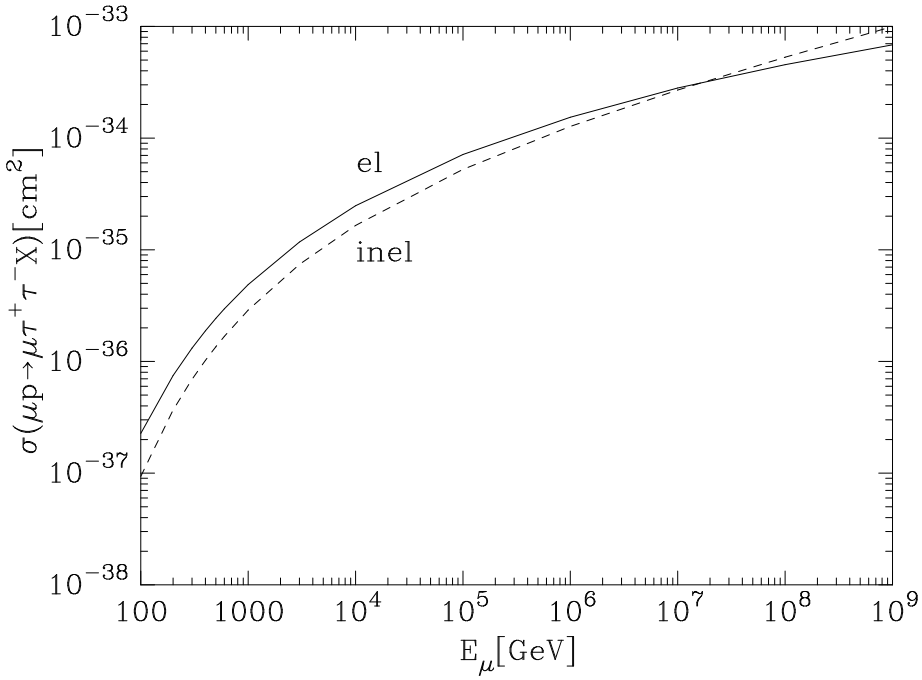

Figure 3.2: Elastic and inelastic contributions to the cross section for $\tau^+\tau^-$ pair production in μp scattering as a function of initial muon energy.

The different scattering contributions to the total cross section have a different energy profile for $\tau^+\tau^-$ pair production as seen in Figure 3.3 (b). For low initial muon energies, $E_\mu = 100 - 1000$ GeV, the contribution to the total cross section from incoherent nucleon scattering is comparable to the contribution from coherent scattering with the nucleus. This can be understood by looking at the t dependence of the Pauli suppression factor in Eq. (2.41) and the approximate expression for t_{min} in Eq. (2.15). For low initial muon energies, t_{min} is large for $\tau^+\tau^-$ pair production. Because of this, the Pauli suppression factor $C(t) \approx 1$ and incoherent nucleon scattering effects contribute a significant amount to the total cross section. As the initial muon energy grows, t_{min} decreases and we expect to see the Pauli suppression of incoherent nucleon contribution.

Another interesting feature of the cross section for $\tau^+\tau^-$ production in Figure 3.3 (b) is the incoherent electron scattering contribution. The energy threshold to

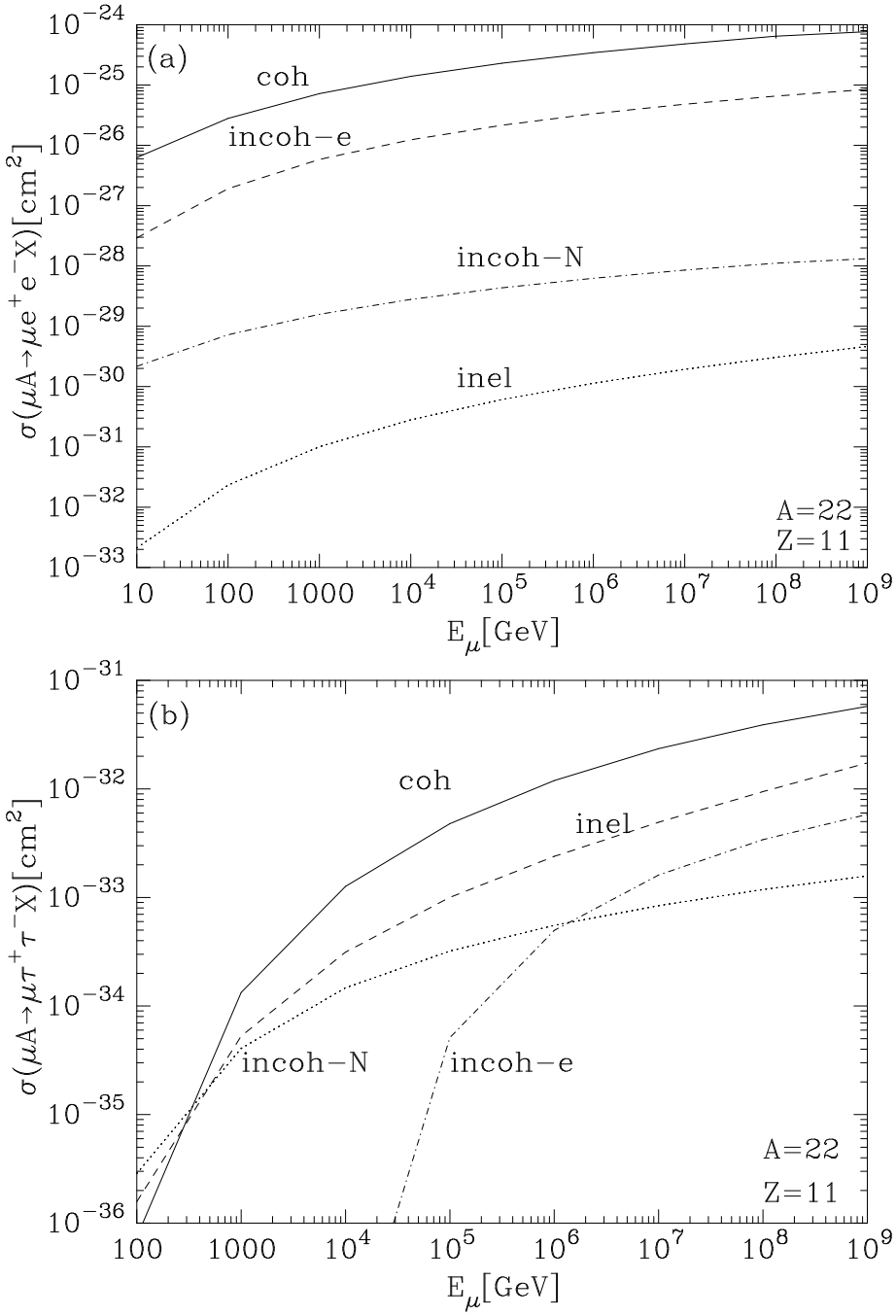

Figure 3.3: Contributions to the total cross section for (a) $\mu A \to \mu e^+ e^- X$ and (b) $\mu A \to \mu \tau^+ \tau^- X$ for standard rock ($Z = 11$, $A = 22$) targets from coherent, incoherent, and inelastic scattering.

produce tau pairs off of electron targets is $E_\mu = 1.24 \times 10^4$ GeV. Once this threshold is reached, the cross section for incoherent electron scattering grows rapidly and at muon energy $E_\mu = 10^9$ GeV it contributes $\sim 10\%$ to the total cross section. Inelastic scattering also contributes significantly to the total cross section for $\tau^+\tau^-$ pair production from muons scattering off of high Z targets, as was the case for proton targets.

In addition to looking at the different contributions to the total cross section, it is also instructive to look at the dependence of the total cross section on the atomic number of the medium being traversed. Figure 3.4 shows the total cross section divided by atomic number for electron-positron pair production from muons scattering with a variety of atomic targets. Because the contribution from coherent scattering with the nucleus, which is proportional to Z^2, provides the dominant contribution to the total cross section, there is still an increase in the total cross section after it has been normalized by dividing out the atomic number for higher Z targets.

3.2 Energy Loss

The electromagnetic energy loss parameter β is defined by the equation

$$\beta = \frac{N_A}{A} \int v \frac{d\sigma}{dv} \ . \tag{3.3}$$

Here, N_A is Avogadro's number, A is the atomic number of the medium being traversed, and v is the fractional energy loss of the incident muon. In the rest frame of the target, the fractional energy loss can be expressed in terms of the initial and final muon energies, $v = (E_\mu - E'_\mu)/E_\mu$. The energy dependence of the different scattering contributions to the energy loss parameter β_{pair} is similar to that of the total cross section. Figure 3.5 shows the elastic and inelastic contributions to the energy loss parameter β_{pair} for electron-positron pair production as a function of

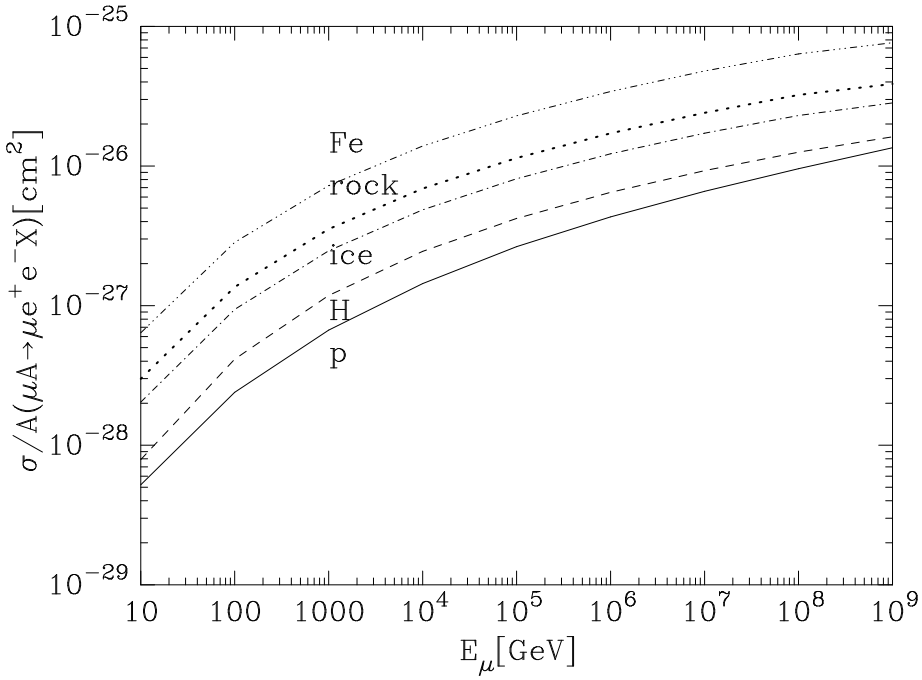

Figure 3.4: Cross section divided by atomic number A for $\mu A \to \mu e^+ e^- X$ as a function of initial muon energy E_μ. Shown are proton ($A = 1$), hydrogen ($A = 1$), ice ($A = 14.3$), standard rock ($A = 22$), and iron ($A = 55.847$) targets.

initial muon energy for muons interacting with proton targets. As can be seen in the plot, the elastic scattering contribution dominates while the contribution from inelastic scattering is suppressed by ~ 4 orders of magnitude for muon energies between 10 GeV $\leq E_\mu \leq 10^8$ GeV.

For $\tau^+\tau^-$ pair production, the contribution from inelastic scattering is comparable to that of elastic scattering. Figure 3.6 shows the contributions from elastic and inelastic scattering for $\tau^+\tau^-$ pair production for muons interacting with proton targets. As can be seen in the plot, inelastic scattering contributes $\sim 30\%$ to the energy loss parameter β_{pair} at $E_\mu = 100$ GeV and steadily increases with increasing initial muon energy. At $E_\mu = 10^9$ GeV, inelastic scattering is the dominant source of energy loss for $\tau^+\tau^-$ pair production, contributing $\sim 80\%$ to β_{pair} for muon production of $\tau^+\tau^-$ pairs.

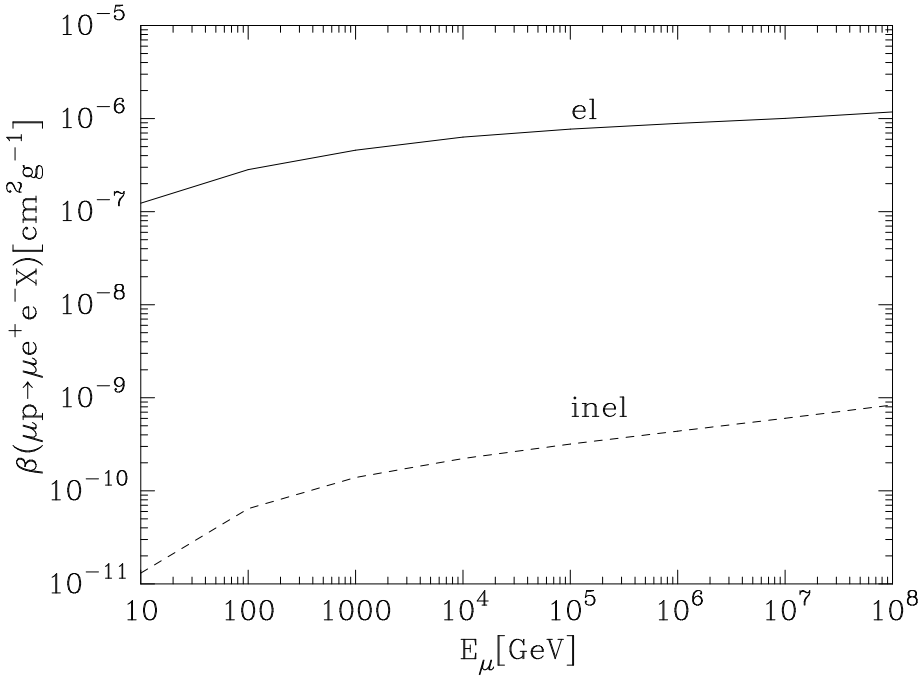

Figure 3.5: Elastic and inelastic contributions to the energy loss parameter β_{pair} for e^+e^- pair production in μp scattering as a function of initial muon energy E_μ.

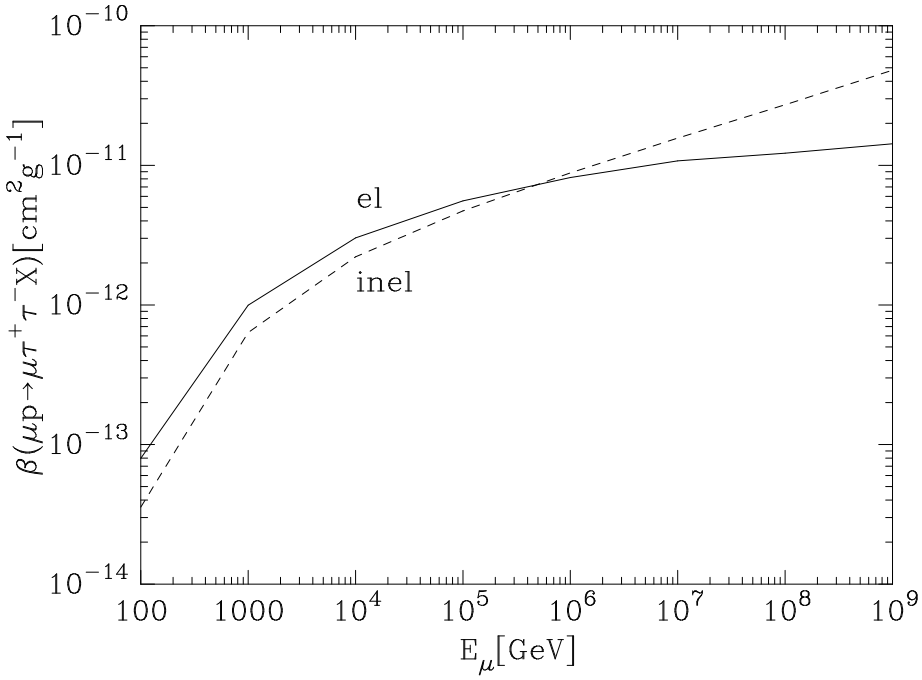

Figure 3.6: Elastic and inelastic contributions to the energy loss parameter β_{pair} for $\tau^+\tau^-$ pair production in μp scattering as a function of initial muon energy E_μ.

Because we are usually interested in energy loss of muons as they transit material, it is useful to look at the energy loss parameter for heavier atomic targets. A plot of the energy loss parameter β_{pair} for electron-positron pair production from muons scattering with atomic targets as a function of initial muon energy is shown in Figure 3.7. For proton targets, β_{pair} grows steadily as a function of energy. This is not the case, however, for high Z targets. For high Z targets, the dominant contribution to β_{pair} in e^+e^- pair production comes from coherent scattering off of the nucleus, as was the case for the total cross section. As the energy of the incoming muon increases, t_{min} decreases (Eq. 2.15). Low t values correspond to large distances. At large distances, screening effects from the bound electrons start to become important and you see an overall decrease in the energy loss for high Z targets at large initial muon energies.

Our results for the energy loss parameter β_{pair} from electron-positron pair production agree well with the commonly used results of Kokoulin and Petrukin (KP) [18, 19]. At initial muon energy $E_\mu = 10$ GeV, our result is 2.5% lower than the result from KP for muons interacting with standard rock. At $E_\mu = 100$ GeV, our results agree to within $< 1\%$, falling to $\sim 4\%$ lower than those of KP at $E_\mu = 10^8$ GeV. For a large range of initial muon energies our results agree to within $< 0.1\%$ to the calculation done by Groom, Mokhov, and Striganov [21].

In addition to considering electron-positron pair production, it is also useful to look at energy loss through $\tau^+\tau^-$ pair production in higher Z targets. Figure 3.8 shows the energy loss parameter β_{pair} for $\tau^+\tau^-$ pair production as a function of initial muon energy for muons in transit through standard rock. As can be seen in the plot, for initial muon energies $E_\mu < 10^9$ GeV, there is no drop off in β_{pair} showing that screening effects have not yet become important at this energy. This is in contrast to e^+e^- pair production. This can once again be understood by looking

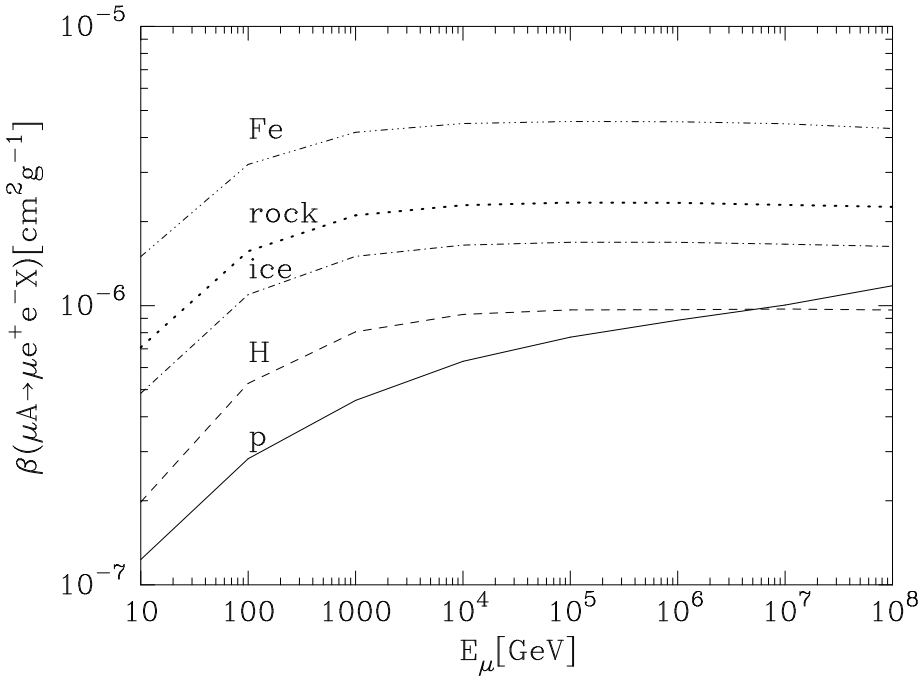

Figure 3.7: Energy loss parameter β_{pair} for proton, hydrogen ($A = 1, Z = 1$), ice ($A = 14.3, Z = 7.23$), rock ($A = 22, Z = 11$), and iron ($A = 55.847, Z = 26$) targets as a function of initial muon energy

at the value of t_{min} for $\tau^+\tau^-$ pair production relative to e^+e^- pair production. Even though β_{pair} grows steadily with increasing muon energy for $\tau^+\tau^-$ pair production in this energy range, the energy loss from $\tau^+\tau^-$ pair production is still suppressed by more than four orders of magnitude relative to the energy loss through e^+e^- pair production at $E_\mu = 10^9$ GeV for standard rock targets. Overall, tau pair production does not significantly contribute to the electromagnetic energy loss of high energy muons for a wide range of atomic targets.

3.3 Differential Cross Section

3.3.1 Direct e^+e^- Pair Production

Using the formalism developed in the Chapter 2, the differential cross section for direct e^+e^- pair production as a function of E_e, the energy of the electron

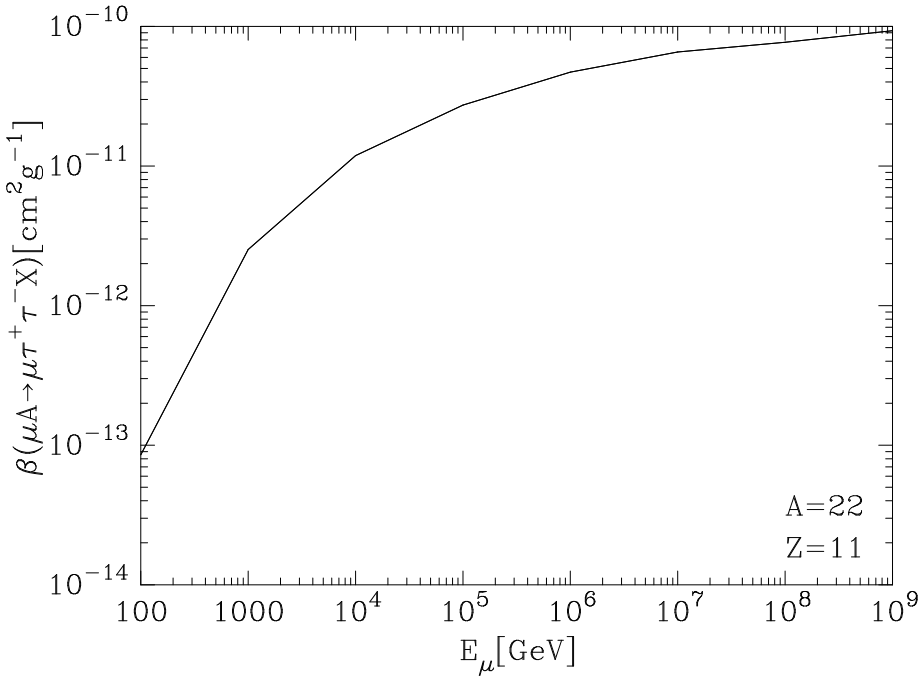

Figure 3.8: Energy loss parameter β_{pair} for $\tau^+\tau^-$pair production as a function of initial muon energy for standard rock, $A = 22$

or positron, can be evaluated numerically. As with the calculation for the total cross section, the differential cross section is dominated by very low momentum transfers to the target. Because of this, the differential cross section is dominated by the contribution from coherent scattering with the nucleus. There is about a 10% contribution which comes from scattering with atomic electrons. For direct production of electron-positron pairs, incoherent scattering with individual nucleons in the target and inelastic scattering give negligible contributions. Because of this, contributions from incoherent nucleon and inelastic scattering effects have been neglected in what follows.

Figure 3.9 shows the differential cross section as a function of electron energy for fixed incident muon energies of 10^3, 10^6, and 10^9 GeV for muons interacting with ice targets ($A = 14.3$). Our numerical results are shown with the solid curves. While we use our numerical results in the calculations to follow, Tannenbaum in

Ref. [22] gives an approximate expression for the differential cross section for lepton pair production as a function of fractional energy transfer $v = (E_\mu - E'_\mu)/E_\mu$ for initial muon energy E_μ and final muon energy E'_μ. For low momentum transfers, $E_\mu - E'_\mu \simeq E_e + E_{\bar{e}}$, the sum of the energies of the produced electron and positron, and $E_e + E_{\bar{e}} \simeq 2E_e$ to first approximation. As a function of v, Tannenbaum has [22]

$$v\frac{d\sigma}{dv} = \frac{28}{9\pi}Z(Z+1)(\alpha r_l)^2\Big[(1+z^2)\ln(1+\frac{1}{z^2}) - 1\Big]f(e,v) \ , \tag{3.4}$$

which can be approximately translated to a distribution in E_e. In the above expression, r_ℓ is the classical radius of the lepton produced and $z = vm_\mu/4m_\ell$. We keep the lepton mass m_ℓ general rather than setting it to m_e to allow a comparison with our numerical results for $\tau^+\tau^-$ pair production. The function $f(e,v)$ is given in two limiting regions [22],

$$f(e,v) = \begin{cases} \ln\Big(vE_\mu/6.67m_l\Big) & \text{unscreened} \\ \ln\Big(184.15m_l/m_eZ\Big) & \text{fully screened}\,. \end{cases} \tag{3.5}$$

To compare our numerical results with the expression given in Eq. (3.4) we have used the lower of the two values for $f(e,v)$.

It is important to note that using the approximation $E_e = vE_\mu/2$, the maximum positron energy that can be used for the differential cross section is $E_\mu/2$. Because we want access to the high energy tail of the distribution we have augmented the value of the fractional energy transfer to be $v \simeq 2E_e/(E_\mu - \frac{1}{2}E_e)$. This is motivated by a comparison of the results obtained using Eq. (3.4) and our numerical results. The expression for v gives the positron energy as

$$E_e = \frac{2v}{4+v}E_\mu \ , \qquad v < 4 \tag{3.6}$$

as a function of v. The dashed curves in Figure 3.9 represent the differential cross section as a function of electron energy using the expressions given in Eqs. (3.4-3.6). As can be seen from the plot, Eq. (3.4) can reproduce our numerical results reasonably well using Eq. (3.6) for the positron energy.

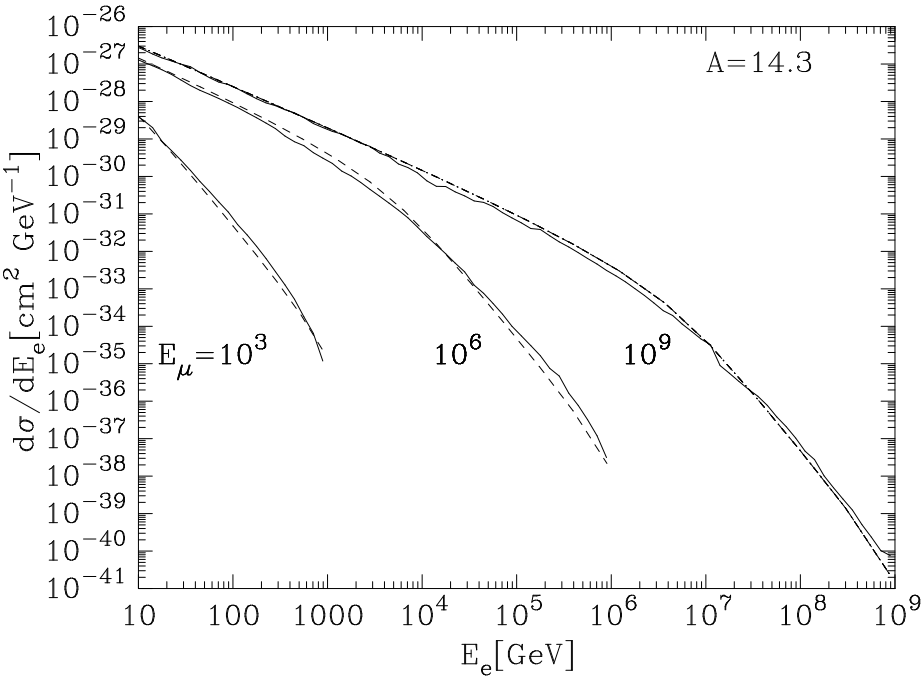

Figure 3.9: Differential cross section as a function of electron energy for $\mu A \to \mu e^+ e^- X$ for fixed muon energies of 10^3, 10^6, and 10^9 GeV. Here $A = 14.3$ and $Z = 7.23$ for ice. The solid lines show our numerical result and the dashed lines show the approximation of Tannenbaum [22] using $v = (E_\mu - E'_\mu)/E_\mu \simeq 2E_e/(E_\mu - E_e/2)$.

3.3.2 Direct $\tau^+\tau^-$ Pair Production

While the previous section has shown that the approximate expression for the differential pair production cross section found in Ref. [22] reproduces our numerical results well for electron-positron pair production, it does not hold for $\tau^+\tau^-$ pair production. As can be seen from Eq. (2.15), t_{min} is proportional to the square of the produced lepton mass. As the mass of the lepton mass increases, so does t_{min}. The approximate expression of Eq. 3.4, while good for low momentum transfers, does not take into account the q^2 evolution of the structure functions. High t values correspond to short distances between the virtual photon and the target. At short distances, the contribution from coherent scattering decrease. Also,

because the lower bound of the momentum transfer increases for heavier lepton production, incoherent nucleon and inelastic scattering effects become increasingly more important for increasing lepton mass.

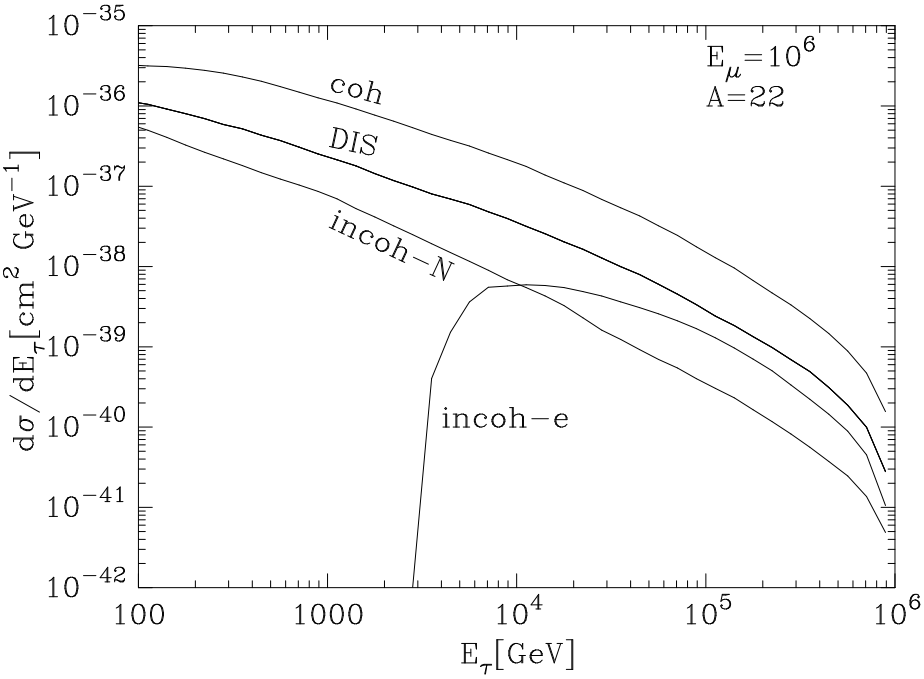

Figure 3.10: Contributions to the differential cross section as a function of tau energy for $\mu A \to \mu\tau^+\tau^- X$ for fixed muon energy, $E_\mu = 10^6$ GeV. Here $A = 22$ and $Z = 11$ is used for standard rock. Indicated are the contributions from coherent scattering with the nucleus (coh), inelastic scattering (DIS), and scattering with individual nucleons (incoh-N) and electrons (incoh-e) in the target.

Figure 3.10 shows the contributions to the differential cross section as a function of tau energy for fixed incident muon energy $E_\mu = 10^6$ GeV in standard rock. The contributions shown are coherent scattering with the nucleus (coh), inelastic scattering (DIS), incoherent scattering with individual nucleons in the target (incoh-N), and incoherent scattering with atomic electrons (incoh-e). As can be seen in the plot, inelastic scattering contributes up to 20% of the total differential cross section for a large range of outgoing tau energies. Incoherent nucleon scattering can also not be ignored for tau pair production. At the lowest tau energies, incoherent nucleon

scattering contributes more than 10% to the differential cross section at this muon energy. Kinematic threshold effects can also be seen in Figure 3.10 when looking at the contribution from scattering off of atomic electrons. Because larger momentum transfers need to be taken into account for $\tau^+\tau^-$ pair production, we can only use our numerical results to evaluate the energy distribution of the differential cross section.

3.3.3 Neutrino Charged Current Interactions

In addition to calculating the energy distribution of the lepton pair production differential cross section, we are also interested in the differential charged current cross section for neutrino nucleon scattering. To be able to compare the expected event rates of leptons entering an underground detector produced via pair production from atmospheric muons with that of single charged leptons produced via charged current interactions from incident atmospheric neutrinos, it is useful to have an approximate form for the charged current differential neutrino cross section.

An approximate form for the differential charged current cross section as a function of inelasticity, $y = 1 - E_\ell/E_\nu$, where E_ℓ is the energy of the produced lepton and E_ν is the incident neutrino energy, can be found in Ref. [53]

$$\frac{d\sigma_\nu}{dy} = \frac{2m_p G_f^2 E_\nu}{\pi}\Big(0.2 + 0.05(1-y)^2\Big) \tag{3.7}$$

$$\frac{d\sigma_{\bar{\nu}}}{dy} = \frac{2m_p G_f^2 E_\nu}{\pi}\Big(0.05 + 0.2(1-y)^2\Big)\ . \tag{3.8}$$

While this approximate form works well for relatively low incident neutrino energies, $E_\nu \leq 10$ TeV, and low energy transfer, it does not take into account the y dependence and energy dependence that comes from an increasing sea quark contribution to the parton distribution functions at higher incident neutrino energies and energy transfers. Because the interest of this work lies with production of high energy leptons that can be measured with large underground detectors, we propose

the following expression for the charged current differential cross section,

$$\frac{d\sigma_{cc}}{dy} = \frac{2m_p G_f^2 E_\nu}{\pi}\Big(a(E_\nu) + b(E_\nu)(1-y)^2\Big)\frac{1}{y^{c(E_\nu)}} \ . \tag{3.9}$$

where we have explicitly included energy dependence in our parameterization. Our parameters $a(E_\nu)$, $b(E_\nu)$, and $c(E_\nu)$ are split into two energy regimes. For neutrino interactions these energy regimes are split by neutrino energy $E_c^\nu = 3.5 \times 10^4$ GeV, and the parameters are given by

$$\begin{aligned} a_\nu &= 0.19 - 0.0265\,(2.214 - \log(E_c^\nu/E_\nu))^2 \\ b_\nu &= 0.036 - 0.0344\,(1.994 - \log(E_c^\nu/E_\nu))^2 \\ c_\nu &= 2.3 \times 10^{-2} \qquad E_\nu < E_c^\nu \ , \end{aligned} \tag{3.10}$$

and for higher energies

$$\begin{aligned} a_\nu &= 0.060\,(E_c^\nu/E_\nu)^{0.675} \\ b_\nu &= 0.169\,(E_c^\nu/E_\nu)^{0.73} \\ c_\nu &= 0.66 \times 10^p \\ p &= 1.453(\log(E_c^\nu)/\log(E_\nu))^{6.24} \qquad E_\nu > E_c^\nu \ . \end{aligned} \tag{3.11}$$

For antineutrino scattering the energy regimes are split by antineutrino energy $E_c^{\bar\nu} = 1 \times 10^6$ GeV. The low energy parameters are given by

$$\begin{aligned} a_{\bar\nu} &= 4.89 \times 10^{-2} \times 10^{p_a} \\ p_a &= -6.31 \times 10^{-4} \log(E_{\bar\nu})^{4.05} \\ b_{\bar\nu} &= 0.177 \times 10^{p_b} \\ p_b &= -2.78 \times 10^{-5} \log(E_{\bar\nu})^{5.9} \\ c_{\bar\nu} &= 4.4 \times 10^{-3} E_{\bar\nu}^{0.32} \qquad E_{\bar\nu} < E_c^{\bar\nu} \ . \end{aligned} \tag{3.12}$$

Because the charged current cross section is dominated by the contribution from sea quarks at high energy, we use the same parameters for high energy ($E_{\bar\nu} \geq 10^6$

GeV) antineutrino scattering as we use for neutrino scattering, Eq. (3.11).

To check the validity of our parameterization, we have also calculated the differential charged current cross section for neutrinos scattering with isoscalar nucleons using the CTEQ6 parton distribution functions [54]. For very small Bjorken x, our numerical results use a power law extrapolation according to $xq(x, Q^2) \sim x^{-\lambda}$ [55, 56]. Figure 3.11 shows the results from our parameterization given in Eq. (3.9) with the parameters given in Eqs. (3.10-3.11) for neutrino isoscalar nucleon scattering compared to the numerical results for neutrino energies from 50 GeV $\leq E_\nu \leq 10^{12}$ GeV. The solid lines show the numerical results while the dashed lines are for our parameterization. Figure 3.12 shows the same for antineutrino nucleon scattering using the parameters given in Eqs. (3.11-3.12).

As can be seen from the two plots, our parameterization for the differential cross section for neutrino and antineutrino charged current interactions with isoscalar nucleons is quite good for a large range of incident energies and energy transfers. For neutrino energies from 50 GeV $\leq E_\nu \leq 10^{12}$ GeV, our parameterization for the y distribution of the differential cross section yields results that are within about 15% of the numerical results found using the CTEQ6 parton distribution functions [54] over the entire range of y values considered.

It is important to note that, in general, the charged current neutrino cross section depends on the mass of the lepton produced. These effects depend on the incident neutrino energy. At incident neutrino energy $E_\nu = 100$ GeV, the charge current cross section for $\nu_\tau N$ scattering is about 80% of that for $\nu_\mu N$ scattering for isoscalar nucleon N [57, 58]. This mass effect decreases with increasing incident neutrino energy. At $E_\nu = 1$ TeV, the $\nu_\tau N$ to $\nu_\mu N$ ratio is 0.95. Because this work deals with high energy leptons, we neglect the effect of lepton mass corrections in our parameterization of the charged current differential cross section.

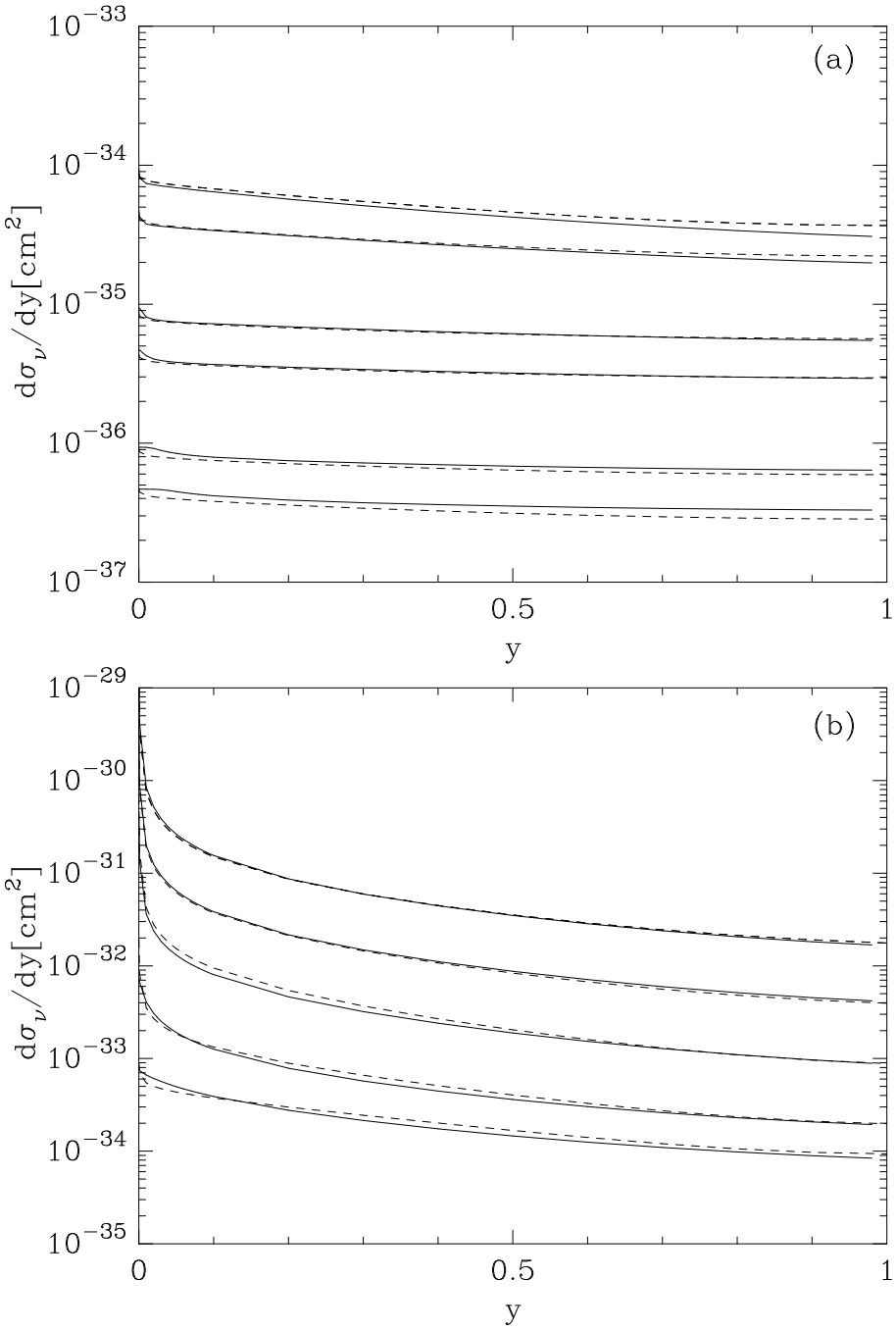

Figure 3.11: Differential neutrino-nucleon cross section defined by Eq. 3.9 with parameters from Eqs. (3.10-3.11). The solid lines represent numerical results using the CTEQ6 parton distribution functions [54] and the dashed lines are our approximate analytic formula. Fig. (a) is the differential cross section for $E_\nu \leq 3.5 \times 10^4$ GeV with the fit parameters defined in Eq. (3.10). The curves represent $E_\nu = 50, 100, 500, 1000, 5000, 10^4$ GeV from bottom to top. Fig. (b) is the differential cross section with parameters defined in Eq. (3.11). The curves represent incident neutrino energies $E_\nu = 10^5, 10^6, 10^8, 10^{10}, 10^{12}$ GeV from bottom to top.

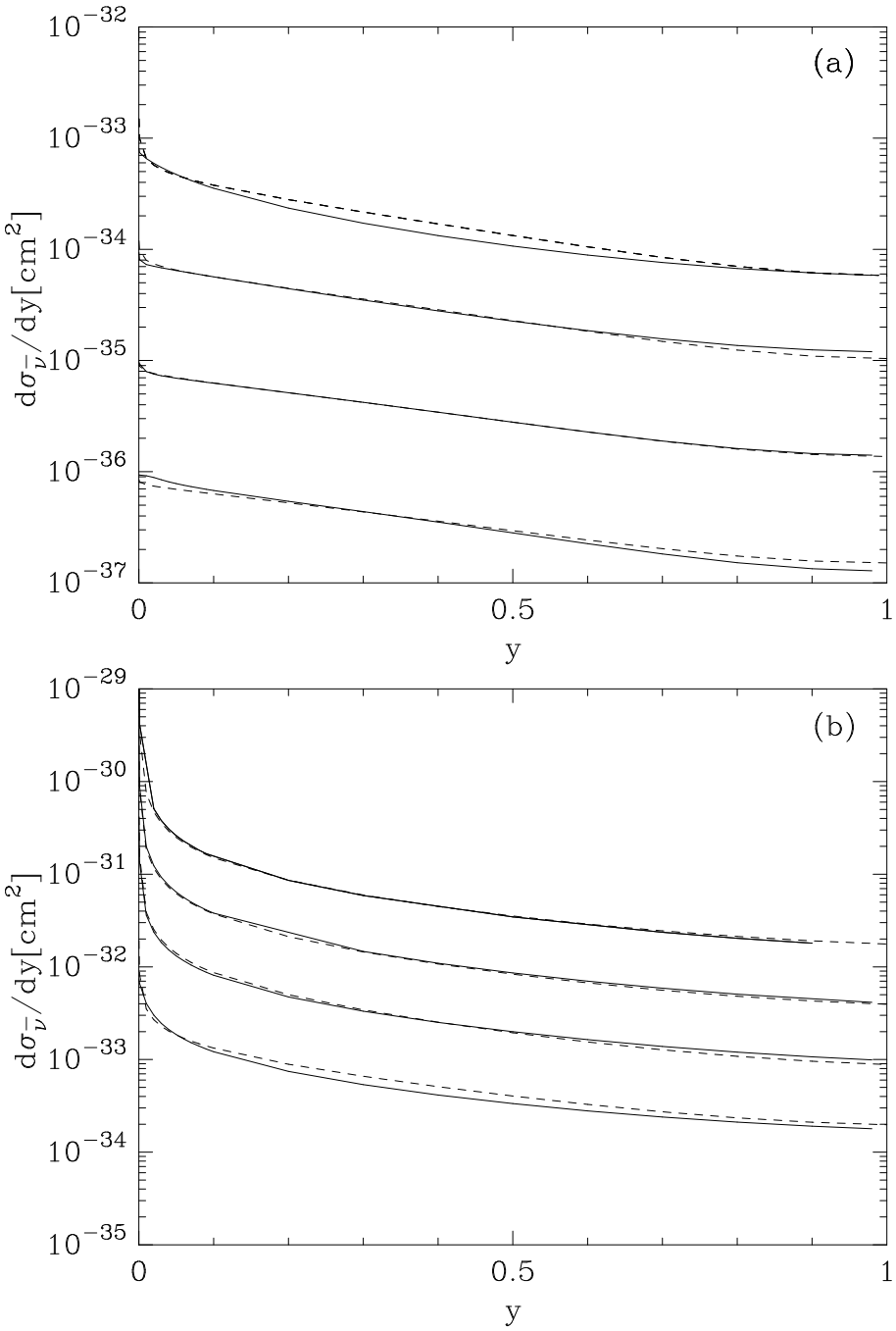

Figure 3.12: Differential antineutrino-nucleon cross section defined by Eq. (3.9). The solid lines represent numerical results using the CTEQ6 parton distribution functions [54] and the dashed lines are the results of our approximate analytic formula. Fig. (a) is the differential cross section for $E_{\bar{\nu}} < 10^6$ GeV with the fit parameters defined in Eq. (3.12). The curves represent incident antineutrino energies of $E_{\bar{\nu}} = 100, 10^3, 10^4, 10^5$ GeV from bottom to top. Fig. (b) is the differential cross section with parameters defined in Eq. (3.11). The curves represent incident antineutrino energies $E_{\bar{\nu}} = 10^6, 10^8, 10^{10}, 10^{12}$ GeV from bottom to top.

CHAPTER 4
ATMOSPHERIC LEPTON FLUXES

4.1 Surface Fluxes

In this chapter, I summarize the parameterizations of the atmospheric lepton fluxes we use in our calculation for production of underground leptons. I discuss both conventional and prompt production of atmospheric leptons. As was discussed previously, the conventional atmospheric flux comes from the decay and interactions of light mesons. The prompt atmospheric flux comes from interactions and decays of heavy mesons. At low energies, conventional production gives the dominant contribution to the atmospheric fluxes at the surface. This is due to the fact that the cross section to produce light quarks is much higher than that to produce heavy quarks. Even though the cross section for heavy meson production is lower than that for light meson production, prompt atmospheric lepton fluxes become the dominant source for atmospheric leptons at the surface at high energy. This can be understood by looking at the decay lengths of mesons. The decay length for pions is 7.8045 m while for D mesons it is 311.8 μm. As the energy of the mesons increase, light mesons do not have a chance to decay before reaching the surface of the earth. Charmed mesons, due to their short decay length, do decay before reaching the surface even at very high energy.

4.1.1 Atmospheric Muon Flux

Following the work of Ref. [2], the conventional muon flux at sea level as a function of zenith angle θ and energy E_μ can be expressed as

$$\begin{aligned} \phi_{\mu+\bar{\mu}}(E_\mu, 0, \theta) &= \frac{0.175\ (\mathrm{GeV\,cm^2\,sr\,s})^{-1}}{(E_\mu/\mathrm{GeV})^{2.72}} \\ &\times \left(\frac{1}{1 + E_\mu \cos\theta^{**}/103\ \mathrm{GeV}} + \frac{0.037}{1 + E_\mu \cos\theta^{**}/810\ \mathrm{GeV}}\right) . \end{aligned} \tag{4.1}$$

The first term in the parenthesis of the above above equation represents the contribution to the conventional atmospheric muon flux from pions created in the atmosphere while the second is the contribution from kaons. The energies 103 GeV and 810 GeV are the pion and kaon critical energies [2] which are defined as $\epsilon_{crit} = m_m h_0 / c\tau_m$ for meson m using scale height $h_0 \simeq 6$ km [5, 6]. The critical energies separate the high and low energy contributions to the atmospheric flux. The low energy contribution to the conventional atmospheric muon flux comes from the decay of light mesons. As the energy increases, the meson decay length becomes longer than the height of the atmosphere and interactions between mesons and air nuclei becomes the predominate source of lepton production. As can be seen from Eq. (4.1), for energies below the GeV range, the atmospheric muon flux scales as $E_\mu^{-2.72}$. As muon energies increase, the scaling becomes $E_\mu^{-3.72}$. This energy scaling behavior comes from the small probability of meson decay relative to reinteraction above the critical energy. In the above equation, $\cos\theta^{**}$ is the effective cosine,

$$\cos\theta^{**} = S(\theta)\cos\theta^{*} \tag{4.2}$$

$$S(\theta) = 0.986 + 0.014\sec\theta \ , \tag{4.3}$$

which takes into account the spherical geometry of the atmosphere [2]. The parameterization for $\cos\theta^{*}$ can be found in Appendix A of Ref. [2].

The prompt atmospheric muon flux is dominated by the decay of charmed mesons. There are many predictions for the prompt muon flux at sea level [3, 5, 7, 11]. Predictions from a perturbative QCD calculation can be parameterized by [7]

$$\log(E_\mu^3 \phi_{\mu+\bar{\mu}}(E,0)) \simeq -5.37 + 0.0191x + 0.156x^2 - 0.0153x^3 \tag{4.4}$$

for x defined by $x \equiv \log(E_\mu/\mathrm{GeV})$. This is not as simple a form as the parameterization for the conventional atmospheric muon flux at sea level found in Eq. (4.1) because it is a fit to numerical results. Also, the energy scaling in the production

of charmed mesons is not as simple as the energy scaling for the production of light mesons. This expression is independent of zenith angle, an approximation valid below 10^7 GeV.

The prompt atmospheric muon flux at sea level can also be calculated using a dipole model evaluation of the $c\bar{c}$ cross section [11]. The approximate form for the prompt muon flux at sea level using this analysis can be found in Ref. [11] and is given by

$$\phi_{\mu+\bar{\mu}}(E_\mu, 0, \theta) \simeq \frac{2.33 \times 10^{-6}\,(\mathrm{GeV\,cm^2\,sr\,s})^{-1}}{(E_\mu/\mathrm{GeV})^{2.53}(1 + E_\mu \cos\theta^{**}/E_0)} \tag{4.5}$$

for $E_0 = 3.08 \times 10^6$ GeV. This evaluation gives a slightly lower prompt muon flux at high energies than that given by Eq. (4.4). It also includes the dependence on zenith angle.

Figure 4.1 compares the conventional atmospheric muon flux given in Eq. (4.1) with the two formulas for prompt muon fluxes given in Eqs. (4.4 & 4.5) at sea level in the vertical direction. As can be seen from the plot, the conventional atmospheric muon flux gives the dominant contribution to the total flux for $E_\mu < 10^6$ GeV, when the prompt flux contributions take over. The zenith angle dependence of Eq. (4.1) has the effect of slightly increasing the sea level flux as the zenith angle increases. This is because larger zenith angles correspond to higher slant depths for the mesons as they penetrate the atmosphere.

4.1.2 Atmospheric Neutrino Fluxes

Because our end goal is to compare underground electron and tau production rates produced through pair production from incident muons with the rates of production for single electrons and taus produced via charged current neutrino interactions, we also need parameterizations for the atmospheric neutrino fluxes. At the energies of interest, $E_\nu > 100$ GeV, the conventional atmospheric electron

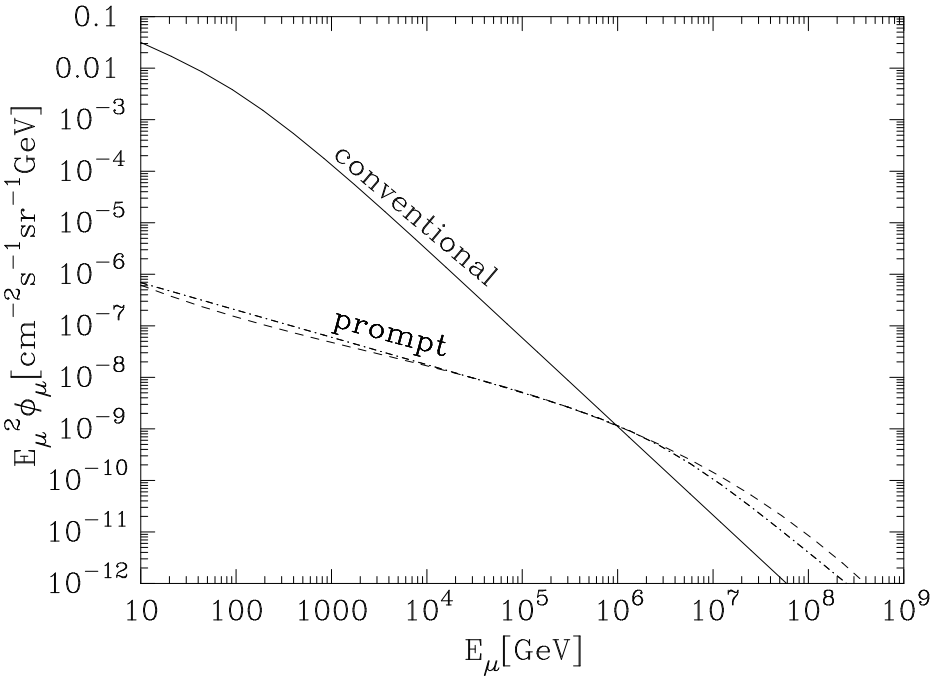

Figure 4.1: Contributions to the atmospheric muon flux at sea level in the vertical direction. The solid curve represents the conventional muon flux given by Eq. (4.1). The dashed curve represents the prompt muon flux calculated from perterbative QCD given by Eq. (4.4) while the dot-dashed curve represents the prompt flux given in Eq. (4.5) calculated using a dipole model of the $c\bar{c}$ cross section.

neutrino flux has approximately the same energy dependence as the conventional muon flux, Eq. (4.1). The normalization is a factor of 135 smaller [59] and for our calculations we use

$$\begin{aligned} \phi_{\nu_e+\bar{\nu}_e}(E_\nu, 0, \theta) &= \frac{1.30 \times 10^{-3}\ (\mathrm{GeV\,cm^2\,sr\,s})^{-1}}{(E_\nu/\mathrm{GeV})^{2.72}} \\ &\times \left(\frac{1}{1 + E_\nu \cos\theta^{**}/103\ \mathrm{GeV}} + \frac{0.037}{1 + E_\nu \cos\theta^{**}/810\ \mathrm{GeV}}\right) . \end{aligned} \tag{4.6}$$

for the conventional flux of $\nu_e + \bar{\nu}_e$. At neutrino energy $E_\nu = 1$ TeV the conventional flux of neutrinos to antineutrinos has an approximate 60:40 ratio [59]. For simplicity, we use this ratio for the full energy range under consideration.

For the prompt atmospheric electron neutrino flux we use the same approximate formulas as those for the prompt atmospheric muon flux found in Eqs. (4.4

& 4.5). This is due to the fact that charmed mesons decay into electronic and muonic channels with an equal branching ratio. Also, the energy distribution of the lepton and neutrino produced in charm decay is about the same. For the prompt atmospheric electron neutrino flux, the ratio of ν_e to $\bar{\nu}_e$ is 50:50.

For the atmospheric tau neutrino flux in the downward direction, two sources need to be considered. The first is neutrino oscillations. The primary contribution comes from $\nu_\mu \to \nu_\tau$ oscillations. In the present analysis we are considering downward fluxes ranging from the vertical direction to a zenith angle of 45° for neutrino energies in the TeV and above range. The average height of production for leptons in the atmosphere is $\sim$ 15 km [8]. The probability for neutrino oscillations depends on the function

$$\sin^2\left(1.27\Delta m^2(\mathrm{eV}^2)\frac{L(\mathrm{km})}{E_\nu(\ \mathrm{GeV})}\right) \ . \tag{4.7}$$

At the energies and distances of interest here, the argument of the above function is small, therefore there is not a significant contribution to the downward going tau neutrino flux from neutrino oscillations. Because of this, we neglect neutrino oscillations as a source of tau neutrinos.

The other source of downward going tau neutrinos is the decay of D_s and b mesons and subsequent tau decays [3, 4]. An approximate form for the prompt tau neutrino flux from this production mechanism can be found in Ref. [4],

$$\begin{aligned}\phi_{\nu_\tau+\bar{\nu}_\tau}(E_\nu,0) &= \frac{1\times10^{-7}E_\nu^{0.5}\ (\mathrm{GeV\,cm^2\,sr\,s})^{-1}}{(E_\nu/\mathrm{GeV})^3} \\ &\times \left(\frac{1}{1+(E_\nu/1\times10^6)^{0.7}+(E_\nu/4\times10^6)^{1.5}}\right) .\end{aligned} \tag{4.8}$$

As is the case for prompt production of electron neutrinos and antineutrinos, the ratio for tau neutrinos to antineutrinos is 50:50.

4.2 Depth Corrections

When considering the atmospheric muon flux at depth, electromagnetic energy losses of the muon need to be taken into account [6, 21]. The general energy loss formula for muons in transit is given by

$$-\langle \frac{dE}{dX} \rangle = \alpha + \sum_{i}^{3} \beta_i E \tag{4.9}$$

for column depth X. Using the above equations, the atmospheric muon flux at depth d can be written as

$$\phi^{cl}_{\mu+\bar{\mu}}(E_\mu, d, \theta) \simeq \phi_{\mu+\bar{\mu}}(E^s_\mu, 0, \theta) \exp(\beta \rho d) \tag{4.10}$$

for muons traveling through material of constant density ρ. In the above equation, E^s_μ denotes the surface energy. The vertical depth d and the column depth X are related through $X = \rho d$ when the density is constant. The above formula assumes continuous energy loss (cl). It is known that fluctuations in energy loss lead to an increase in the down-going atmospheric flux at depth [20], however, this amounts to only a $5\% - 10\%$ increase in the flux at a depth of 1 km water equivalent for muon energies from 100 GeV $-$ 1 TeV [2]. In what follows, we neglect the effects of energy loss fluctuations. As a side note, water equivalent distance is related to vertical depth through the slant depth. For example, 1 km water equivelent is equal to a slant depth of 10^5 g/cm^2 which corresponds to a depth $d = 10^5/\rho \simeq 3.8 \times 10^4$ cm of rock ($\rho_{std\ rock} = 2.65$ g/cm^3).

The relationship between the surface energy and the energy of the muon at depth d can be found by integrating Eq. (4.9) assuming constant α and β and is given by

$$E^s_\mu = \exp(\beta \rho d) E_\mu + (\exp(\beta \rho d) - 1) \frac{\alpha}{\beta} \ . \tag{4.11}$$

The exponential factor in Eq. (4.10) comes from differentiating the above expression

$$\frac{dE_\mu^s}{dE_\mu} = \exp(\beta\rho d) \ . \tag{4.12}$$

To determine the atmospheric muon flux at depth, we use the approximate two slope linear fit from Ref. [2] for the energy loss parameters,

$$\begin{aligned} \alpha &= 2.67 \times 10^{-3}\mathrm{GeVcm}^2/\mathrm{g} \\ \beta &= 2.4 \times 10^{-6}\mathrm{cm}^2/\mathrm{g} \end{aligned} \tag{4.13}$$

for $E_\mu \leq 3.53 \times 10^4$ GeV, and

$$\begin{aligned} \alpha &= -6.5 \times 10^{-3}\mathrm{GeVcm}^2/\mathrm{g} \\ \beta &= 3.66 \times 10^{-6}\mathrm{cm}^2/\mathrm{g} \end{aligned} \tag{4.14}$$

at higher muon energies. Figure 4.2 shows the contributions to the underground atmospheric muon flux at a depth of 1.5 km in ice. As was the case for the atmospheric muon flux at the surface, the prompt flux becomes the dominant contribution to the underground flux for muon energies $E_\mu > 10^6$ GeV.

When considering fluxes of atmospheric leptons at depth coming from higher zenith angles there are competing effects that need to be considered. The first is the increase of the atmospheric flux at the surface of the earth. Higher zenith angles lead to a higher slant depth ($D \to D/\cos\theta$) in the atmosphere. The higher slant depth leads to an increase in the number of decays of light mesons at high energies. For example, the conventional atmospheric muon flux at the surface increases by a factor of ~ 2 for $E_\mu = 10^6$ GeV when the zenith angle increases from $0^\circ \to 60^\circ$. There is also an increase in the atmospheric flux of neutrinos and antineutrinos with increased zenith angle. The second effect that needs to be accounted for is the electromagnetic energy loss of muons in transit. The effect of muon energy loss on the downward going atmospheric muon flux at depth is governed by Eq. (4.10). Even though the surface flux increases with increasing zenith angle, there is a net

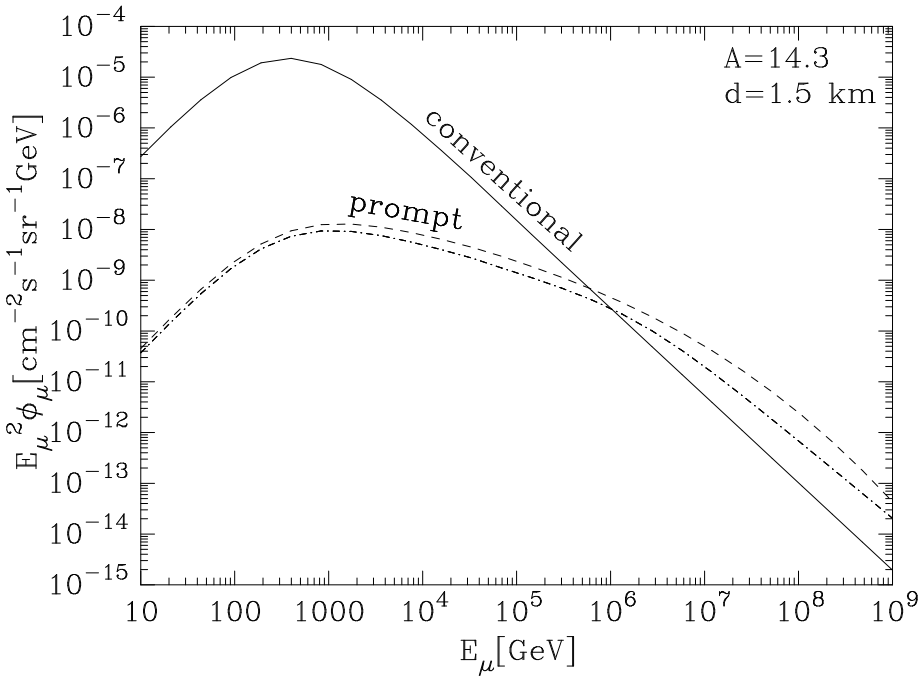

Figure 4.2: Contributions to the atmospheric muon flux at a depth of 1.5 km in ice, $A = 14.3$. The solid curve represents the conventional muon flux given in Eq. (4.1). The dashed curve represents the prompt flux given by Eq. (4.4) while the dot-dashed curve represents the prompt flux given in Eq. (4.5).

decrease in the atmospheric flux at depth due to electromagnetic energy losses of the muons.

In addition to considering lepton production underground, we are also interested in lepton production in the mountains surrounding the High Altitude Water Cherenkov (HAWC) surface array. This proposed array sits in a saddle at an altitude of 4.1 km, shielded on two sides by mountains. The atmospheric flux at this altitude is approximately the same as at the surface. This is due to the fact that the average height of production for mesons produced in cosmic ray-air nuclei collisions is approximately 15 km [8]. At altitudes between 15 and 4 km, pion and kaon interactions with air nuclei are favored over decay at the energies of interest here, $E > 10$ GeV.

We are interested in comparing underground lepton production rates from

incident muons with those from incident neutrinos at depth. As was discussed in the previous section, at the energies under consideration here, neutrino oscillations are not an important source of neutrino disappearance between the surface and a depth of 1.5 km under ice. Because of the long interaction length of neutrinos, neutrino attenuation is also not important for the vertical neutrino flux in these regions [55]. The long interaction length of neutrinos also makes the effects from increased zenith angle negligible for underground attenuation of the atmospheric flux. We use the same expressions for the atmospheric neutrino flux at depth as we use for the surface fluxes.

CHAPTER 5
UNDERGROUND LEPTON PRODUCTION

5.1 Event Geometries

Before describing the formalism used to calculate underground production of leptons, it is instructive to describe the types of event geometries being considered. Figure 5.1 shows the three types of events being considered for the detectors IceCube and HAWC. Figures 5.1 (a) and (b) represent events for the IceCube detector. Here, the circle represents the earth while the embedded square is the detecting volume of IceCube. For underground electron production, we are looking at contained events in IceCube. Contained events correspond to particle production and decay inside the detector. This is shown Figure 5.1 (a). For tau production, we consider two types of event geometry. The first, shown in Figure 5.1 (b), corresponds to tau events in IceCube. Here, tau particles are produced outside of, then enter, the detecting volume. The second, shown in Figure 5.1 (c), represents tau production for the HAWC array. Tau particles are produced in the mountains surrounding the surface array, then they exit the mountain above the detector. For low enough energy, the exiting taus will decay in the air above the detector, producing a shower. The events shown in Figure 5.1 correspond to leptons produced via pair production from atmospheric muons. For lepton production from atmospheric neutrinos, there is only a single lepton produced and no outgoing neutrino.

5.2 Underground Electron Production

I begin my discussion of underground lepton production with the formalism used to calculate the differential electron flux produced underground. The formula for the differential flux of electrons produced in a detector (contained) beginning at depth D and extending to depth $D + L_{max}$ from an incident flux of atmospheric

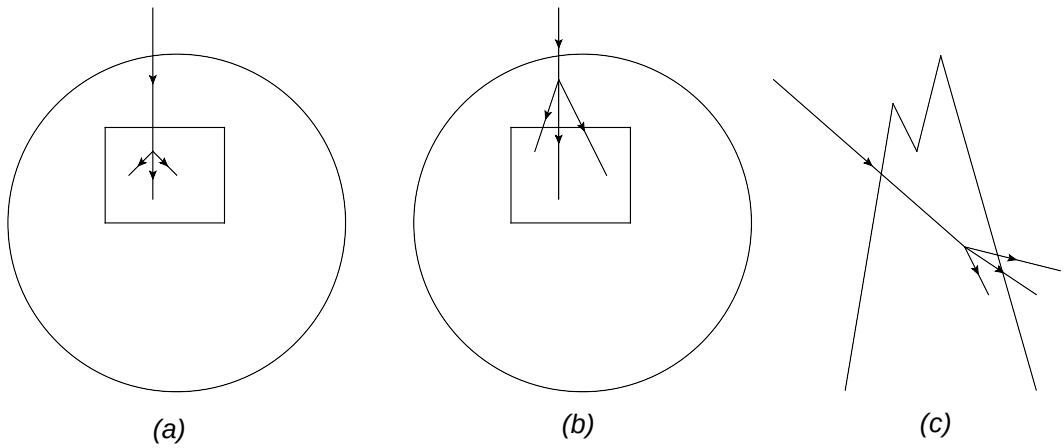

Figure 5.1: The three types of event geometries considered here for underground lepton production by atmospheric muons. Figures (a) and (b) are the types of events being considered for IceCube. Figure (a) represents contained events, i.e., particle production and decay contained in the detector. Figure (b) represents particles produced outside of the detector with the particles then entering the detector vertically. Figure (c) is the type of events being considered for HAWC. Leptons are produced in and then exit the mountains surrounding the surface array.

muons can be expressed as [9]

$$\frac{dN}{dE_e^f} = \int_0^{L_{\max}} d\ell \int_{E_e^i}^{\infty} dE_\mu \int dE_e^i \frac{dP_{\text{prod}}}{d\ell} \phi_{\mu+\bar{\mu}}(E_\mu, D+\ell, \theta)\delta(E_e^f - E_e^i) \ , \tag{5.1}$$

where E_μ is the muon energy at depth and $\phi_{\mu+\bar{\mu}}(E_\mu, D+\ell, \theta)$ is the atmospheric muon flux at depth given in Eq. (4.10). For electrons, the delta function identifies the final energy E_e^f with the initial energy E_e^i. The probability for a muon of energy E_μ to produce an electron with energy E_e^i via pair production in a depth interval $d\ell$ can be written as [9, 60]

$$P_{\text{prod}}(\mu \to e, E_\mu, E_e^i) = d\ell dE_e^i \frac{N_A}{A} \rho \frac{d\sigma_{pair}(E_\mu, E_e^i)}{dE_e^i} \ . \tag{5.2}$$

Here, N_A is Avogadro's number and A is the atomic mass of the material the muon is traversing. Substituting the above expression into Eq. (5.1) and using the delta function to do the integral over the initial electron energy, E_e^i, yields

$$\frac{dN}{dE_e^f} = \int_0^{L_{\max}} d\ell \int_{E_e^f}^{\infty} dE_\mu \frac{N_A}{A} \rho \frac{d\sigma_{pair}(E_\mu, E_e^f)}{dE_e^f} \phi_{\mu+\bar{\mu}}(E_\mu, D+\ell, \theta) \tag{5.3}$$

for the differential electron flux produced by incident atmospheric muons underground.

The above formula is general and can be used to calculate the underground electron flux produced from an incident atmospheric flux of electron neutrinos. For production of single electrons or positrons from incident electron neutrinos and antineutrinos, one needs to replace the differential pair production cross section, $d\sigma_{pair}(E_\mu, E_e^i)/dE_e^i$, with the charged current differential neutrino cross section, $d\sigma_{CC}(E_\nu, E_e^i)/dE_e^i$ defined in Eqs. (3.9-3.12), in the expression for production probability. The atmospheric muon flux at depth also needs to be replaced with the atmospheric electron neutrino flux.

5.2.1 Electron Production in IceCube

For underground production of electrons and positrons, we have focused our calculation on the large underground Cherenkov detector IceCube. The instrumentation at IceCube begins approximately 1.5 km under ice and extends to a depth of approximately 2.5 km. Figure 5.2 shows the differential flux of electrons produced via pair production from incident atmospheric muons compared to the differential flux of single electrons produced via charged current interactions from an incident flux of atmospheric neutrinos. Also shown in the plot are the contributions from both incident conventional and prompt atmospheric fluxes. The differential electron flux shown is that produced between depths of 1.5 km $\leq d \leq$ 2.5 km in ice in the vertical direction.

To understand the comparison of the flux of underground electrons produced from incident atmospheric muons with those produced from incident atmospheric neutrinos, it is important to look at the production mechanism. The production mechanism for electrons produced by atmospheric muons is pair production, i.e., $\mu A \rightarrow \mu e^+ e^- X$. Therefore, the total number of high energy events comes from the

sum of the $\mu + \bar{\mu}$ atmospheric flux. Every electron produced is accompanied by a positron, a muon, and possibly a signal of the interaction. This is in contrast to electrons produced via charged current interactions from incident atmospheric neutrinos. For neutrino production of underground electrons and positrons, the electron signal comes purely from the incident neutrino flux while the positron signal comes purely from the incident antineutrino flux. Because IceCube has no way of measuring the charge of particles produced in the detector, we have summed the event rates of electrons and positrons produced from incident neutrinos and antineutrinos in Figure 5.2 to better compare with the event rates of electrons and positrons produced from incident muons.

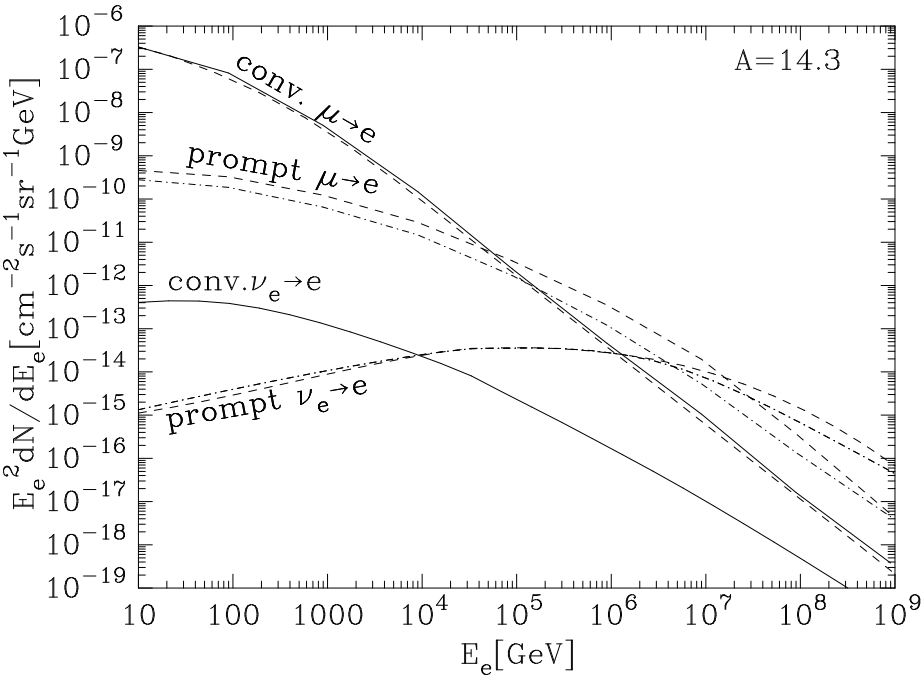

Figure 5.2: The differential underground electron flux scaled by the square of the electron energy for electrons produced in ice between the vertical depths $1.5 \leq d \leq 2.5$ km. The solid curves represent the electron flux produced by incident vertical conventional fluxes of muons and neutrinos given by Eqs. (4.1 & 4.6). The dashed curves labeled prompt represent the contribution from an initial prompt flux given by Eq. (4.4) while the dot-dash curve is the contribution from the prompt flux given in Eq. (4.5). The dashed curve following the conventional $\mu \to e$ curve was calculated using the Tannenbaum approximation to $d\sigma_{pair}/dE_e$.

To understand the curves in Figure 5.2, it is instructive to look at the energy dependence of the incident lepton fluxes in relation to the energy dependence of the differential cross section. Both the incident conventional atmospheric flux of muons and the conventional atmospheric flux of electron neutrinos and antineutrinos scale approximately as E^{-4} at the energies of interest here ($E > 10$ GeV). Because of this, the differential flux of electrons produced underground is dominated by the high energy tails of the energy distributions of the differential cross sections, i.e., large v values for $d\sigma_{pair}/dE_e$ and small y values for $d\sigma_{CC}/dE_e$. This is also the case, although not as pronounced, for electrons produced from incident prompt atmospheric fluxes of muons and neutrinos which fall off approximately as E^{-3}.

As can be seen in Figure 5.2, for electrons produced from incident muons, the underground flux is dominated by the contribution from the conventional atmospheric muon flux for energies $E_e \leq 10^4$ GeV. At higher energies, $E_e \geq 10^5$ GeV, the contribution from the prompt muon flux starts to dominate. This crossover occurs one order of magnitude lower than that for the atmospheric muon flux at depth. Figure 4.2 shows that the atmospheric muon flux at depth is dominated by the conventional contribution for muon energies $E_\mu \leq 10^6$ GeV. Because the crossover occurs one order of magnitude lower when looking at underground electrons produced from incident muons, studying the energy distribution of the underground electron signal may augment efforts to measure the onset of the prompt muon flux. For electrons produced via charged current interactions from incident atmospheric neutrinos and antineutrinos, the crossover for the contributions from conventional neutrinos versus prompt neutrinos occurs at an electron energy of $E_e \sim 10^4$ GeV. It is not until an electron energy of $E_e \simeq 10^7$ that the contributions from atmospheric neutrinos and antineutrinos start to dominate the contributions from incident atmospheric muons to the underground electron flux.

It is important to note that when looking at electron and positron signals in an underground Cherenkov detector, the electromagnetic showers produced are very difficult to distinguish from those produced by photons created by muon bremsstrahlung events. Because of this, it is important to calculate the event rate of the muon bremsstrahlung background to compare with the expected event rate of underground electron and positron production.

Figure 5.3 shows the event rate of bremsstrahlung events, coming from $\mu A \rightarrow \mu\gamma X$, compared to pair produced electrons and positrons from incident atmospheric conventional and prompt muon fluxes. As can be seen, the muon bremsstrahlung signal is ~ 2 orders of magnitude larger than the expected signal from pair production events produced in the detector between depths of 1.5 km $\leq d \leq$ 2.5 km. This is the case even though the energy loss parameter β and the total cross section are lower for bremsstrahlung than for electron-positron pair production. This can be understood by looking at the energy distribution of the differential cross section for muon bremsstrahlung in comparison to that for pair production.

Figure 5.4 shows the energy distribution of both the muon bremsstrahlung and the electron-positron pair production differential cross sections for fixed muon energy $E_\mu = 10^6$ GeV in ice. For the muon bremsstrahlung differential cross section, we have used the parameterization of Ref. [61] with the more precise scaling relation of Ref. [62]. Using the more complicated formula of Ref. [35] which includes target excitation effects in the evaluation of the differential cross section amounts to $< 1\%$ correction in the energy distribution for the values of the fractional energy loss, $v_\gamma \simeq E_\gamma/E_\mu$, important here.

Figure 5.4 shows that for large values of fractional energy transfer $v \geq 0.1$, the differential cross section for muon bremsstrahlung dominates the more steeply

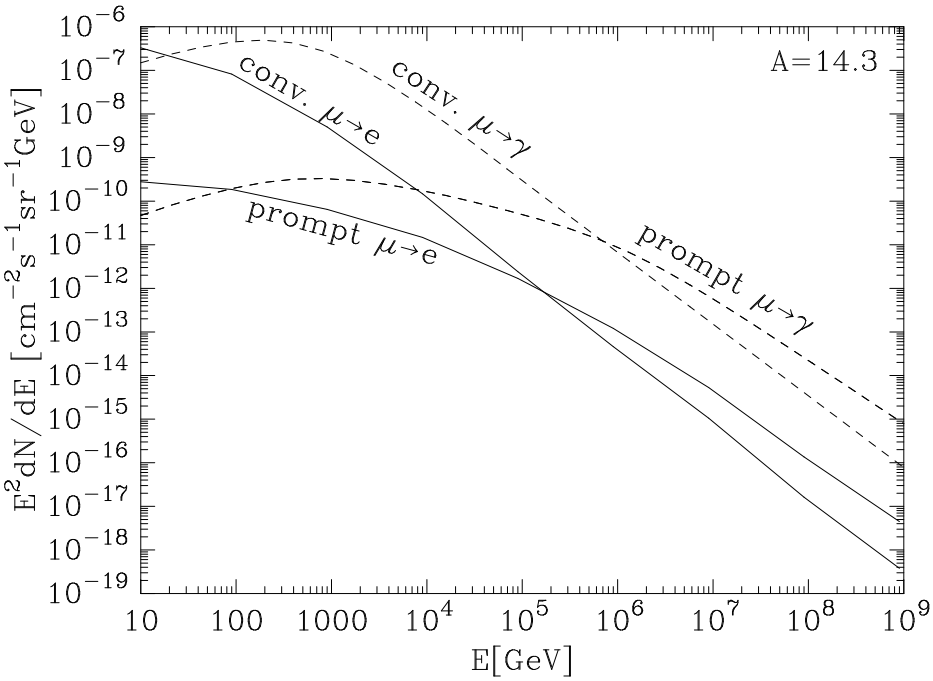

Figure 5.3: The differential underground electron and photon fluxes scaled by the square of the electron or photon energy for particles produced in ice ($A = 14.3$) between the vertical depths $1.5 \leq d \leq 2.5$ km. The solid curves represent the electron flux produced by incident vertical conventional (Eq. (4.1)) and prompt (Eq. (4.5)) atmospheric muons. The dashed curves show the conventional and prompt $\mu \rightarrow \gamma$ contribution.

falling differential pair production cross section. Because the calculation for underground electromagnetic events is dominated by the high energy tail of the differential distribution, as was noted above, bremsstrahlung events are the dominant source of electromagnetic showers produced in underground detectors. It is also important to note that the crossover between conventional and prompt contributions for underground bremsstrahlung events happens at an energy intermediate to that of the underground atmospheric muon flux and the underground electron flux.

In addition to looking at the full electromagnetic signal, it is also instructive to look at the relationship between the initial muon energy and the energy of the produced electron or photon. Because the energy distribution of the differential pair production cross section falls much more steeply than that of the differential

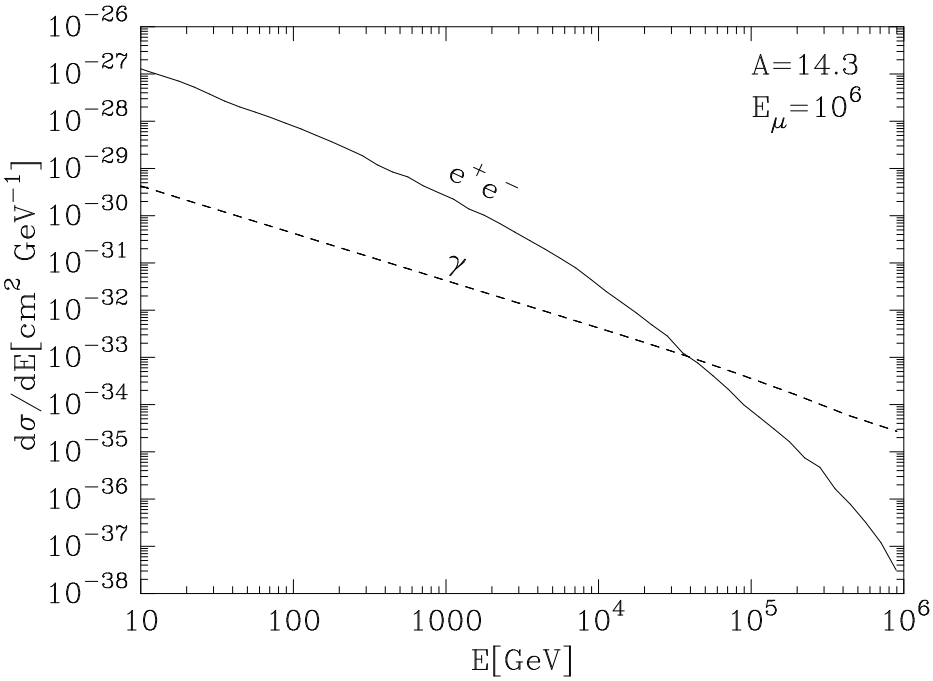

Figure 5.4: Energy distributions for the differential bremsstrahlung cross section for the process $\mu A \to \mu\gamma X$ and the differential electron-positron pair production cross section. The solid curve represents pair production and the dashed curve muon bremsstrahlung. Both of the distributions have been calculated for fixed muon energy $E_\mu = 10^6$ GeV in ice, $A = 14.3$.

bremsstrahlung cross section, higher values of $v_\gamma = E_\gamma/E_\mu$ are favored in relation to v_e. This amounts to a much different v dependence in the underground flux of photons versus electrons. Figure 5.5 shows the underground electron and photon fluxes produced by atmospheric muons where the upper limit of v has been set to $v_{e,(\gamma)}^{max} = 0.01$. With this restriction, the underground photon flux falls by a factor of $\sim 10^5$ whereas the underground electron flux only falls by a factor of $\sim 10^2$. If the initial muon energy could be correlated with the energy of the produced electron or photon with the above restriction, the electron signal coming from electron-positron pair production would be a factor of ~ 10 higher than the corresponding photon signal produced via muon bremsstrahlung. Using this restriction would help to reduce the background from muon bremsstrahlung events when looking for

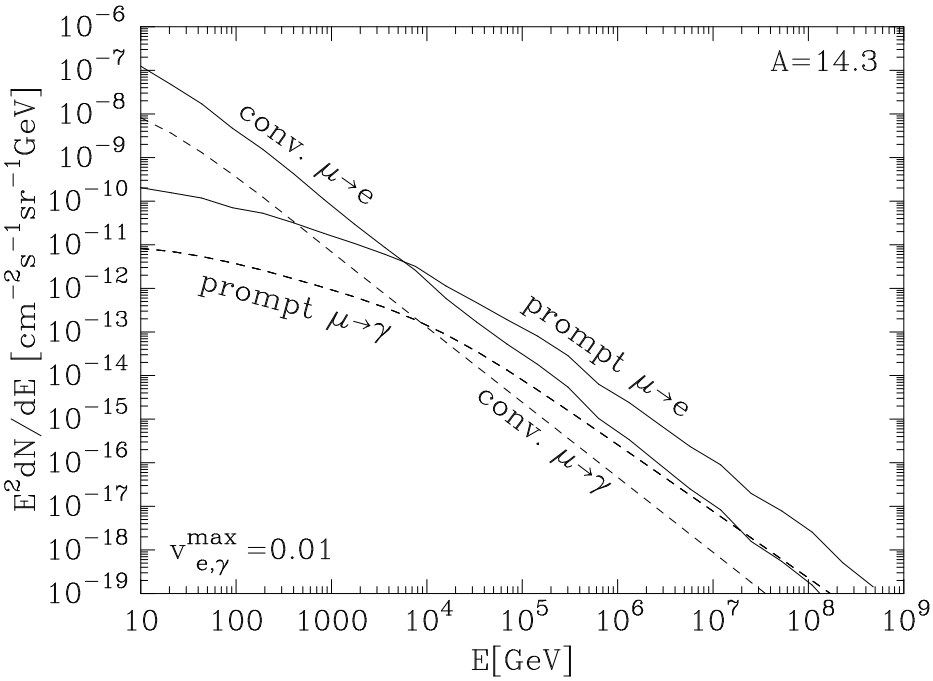

Figure 5.5: The differential flux of electrons and photons scaled by the square of the electron or photon energy calculated using the restriction $v_{e,\gamma}^{max} = 0.01$ ($E_{\mu}^{min} \approx 100 E_{e,\gamma}$). Shown in the plot are the differential flux of electrons and photons produced from both conventional (Eq. (4.1)) and prompt (Eq. (4.5)) incident atmospheric muons.

electron-positron electromagnetic signals in underground detectors.

5.3 Underground Tau Production

For underground electron production, we neglected the energy loss and survival probability of the electrons in our evaluation of the underground differential flux. This is due to the fact that once produced, electrons and positrons shower very quickly. Electrons and positrons must be produced in the detector to be observed. For underground tau signals this is not the case. High energy taus can persist over large distances underground, losing energy electromagnetically as they transit. The electromagnetic energy loss of high energy taus through material is governed by

$$\langle \frac{dE}{dX} \rangle \simeq \frac{dE}{dX} \simeq -\beta_{\tau} E \tag{5.4}$$

assuming continuous energy loss. The energy loss parameter β_τ is a factor of m_μ/m_τ smaller than the energy loss parameter for muons. Using the above equation, the relationship between the initial tau energy and the energy of the tau after traveling a distance ℓ is given by

$$E_\tau^f = E_\tau^i \exp(-\beta_\tau \rho \ell) \tag{5.5}$$

for constant density ρ and β_τ. In what follows, we assume a constant energy loss parameter for standard rock, $\beta_\tau = 8.5 \times 10^{-7}$ cm^2/g [9, 23]. Accounting for the finite lifetime of the tau and electromagnetic energy losses yields a survival probability of [9, 23, 60]

$$P_{\text{surv}}(E_\tau^f, E_\tau^i) = \exp\left[\frac{m_\tau}{c\tau_\tau \beta_\tau \rho}\left(\frac{1}{E_\tau^i} - \frac{1}{E_\tau^f}\right)\right] . \tag{5.6}$$

The relationship between initial and final tau energies is given in Eq. (5.5).

As was noted above, high energy taus can persist over large distances. The decay length of a tau with initial energy $E_\tau^i = 10$ PeV is ~ 500 m. Tau particles that traverse a detector and do not decay in that detector have signals that mimic a muon. Looking at the energy loss relationship, a muon with initial energy $E_\mu^i = \beta_\tau E_\tau^i/\beta_\mu$ will have approximately the same energy loss as a tau with E_τ^i over a given column depth. Because Cherenkov detectors have no way of measuring initial energy of uncontained events, tau events without a decay are indistinguishable from lower energy muon signals. Consequently, it is beneficial to have a understanding of the expected high energy tau background in underground detectors.

Following the formalism of the previous section, and incorporating the energy loss and survival probability of the tau, the differential flux of taus entering a

detector at depth D as a function of energy and zenith angle is given by [9]

$$\begin{aligned}
\frac{dN}{dE_\tau^f} &= \int_0^D d\ell \int_{E_\tau^i}^{E_\tau^i \exp(\beta_\tau \rho(D-\ell))} dE_\tau^{i'} \int_{E_\tau^{i'}}^{\infty} dE_\mu \frac{dP_{\rm prod}}{d\ell} \phi_{\mu+\bar{\mu}}(E_\mu, \ell, \cos\theta) \\
&\times P_{\rm surv}(E_\tau^f, E_\tau^{i'}) \delta(E_\tau^f - E_\tau^{i'} \exp(-\beta\rho(D-\ell))) \\
&= \int_0^D d\ell \int_{E_\tau^i}^{\infty} dE_\mu \frac{N_A}{A} \rho \frac{d\sigma_{pair}(E_\mu, E_\tau^i)}{dE_\tau^i} \phi_{\mu+\bar{\mu}}(E_\mu, \ell, \cos\theta) \\
&\times \exp\Big[\frac{m_\tau}{c\tau\beta_\tau\rho}\Big(\frac{\exp(-\beta_\tau\rho(D-\ell))}{E_\tau^f} - \frac{1}{E_\tau^f}\Big)\Big] \,. \qquad (5.7)
\end{aligned}$$

The delta function in the above equation specifically enforces the energy loss relationship found in Eq. (5.5).

As was the case for the formula used to calculate the differential flux of electrons produced underground, Eq. (5.7) is general and can be used for neutrino induced tau production. For tau neutrino and antineutrino production of tau and antitau particles, the differential pair production cross section in Eq. (5.7) needs to be replaced by the differential charged current cross section defined in Eq. (3.9). Also, the underground incident atmospheric muon flux needs to be replaced with the atmospheric flux of tau neutrinos and antineutrinos.

5.3.1 PeV Taus in IceCube

Atmospheric muons are a background to searches for tau neutrino induced tau events in underground detectors since a tau track without a decay mimics a lower energy muon. Because of this, detectors like IceCube look for contained or partially contained events to identify tau signals. One of the signals used to identify tau particles is the so-called "lollipop" event [12, 63]. This event is identified with an entering electromagnetic tau track and decay that leaves a splash of energy in the detector. The minimum tau energy for "lollipop" events in IceCube is $E_\tau = 5$ PeV [12, 63], which corresponds to a decay length of ~ 250 m.

In addition to the muon background in searches for tau signals, there is also

potential to create taus through the interaction $\mu A \rightarrow \mu\tau^+\tau^- X$. For taus produced in this interaction with high enough energy, there is the potential for taus created outside the detector to enter the detector and subsequently decay. This type of event is a background to charged current production of taus and antitaus from incident tau neutrinos and antineutrinos. To understand the contributions to the underground tau flux, we have calculated the differential flux of taus entering IceCube at a depth of $D = 1.5$ km in the vertical direction. Figure 5.6 shows the contributions to the underground differential flux of taus produced from incident conventional and prompt atmospheric muons as well as the flux of taus produced from incident prompt tau neutrinos and antineutrinos for tau energies of $E_\tau = 1 - 1000$ PeV. In this energy range, the dominant contribution to the underground tau flux comes from incident prompt atmospheric tau neutrinos and antineutrinos. The total underground tau flux receives $\sim 20\%$ contribution from prompt $\mu \rightarrow \tau$ production. In this energy range, the contribution to the underground tau flux from conventional $\mu \rightarrow \tau$ production is suppressed by $1-2$ orders of magnitude relative to the prompt $\nu_\tau \rightarrow \tau$ contribution.

To understand the expected number of "lollipop" events for a given tau flux, it is necessary to look at the survival probability defined in Eq. (5.6) in relation to the decay length of the tau. For taus with energy $E_\tau = 10^5$ GeV, the decay length is approximately 5 m. This means that for a tau of energy $E_\tau = 10^5$ GeV entering the detector, the survival probability of the tau is $P_{surv} \simeq 0$ over the 1 km of detector distance. As tau energy increases, the survival probability increases as well. For taus with energy $E_\tau = 10^8$ GeV entering the detector, the survival probability over the 1 km of detector distance increases to $P_{surv} \simeq 0.8$. The survival probability does not directly correlate to the decay length of the tau entering the detector because electromagnetic energy losses are taken into account as the tau traverses

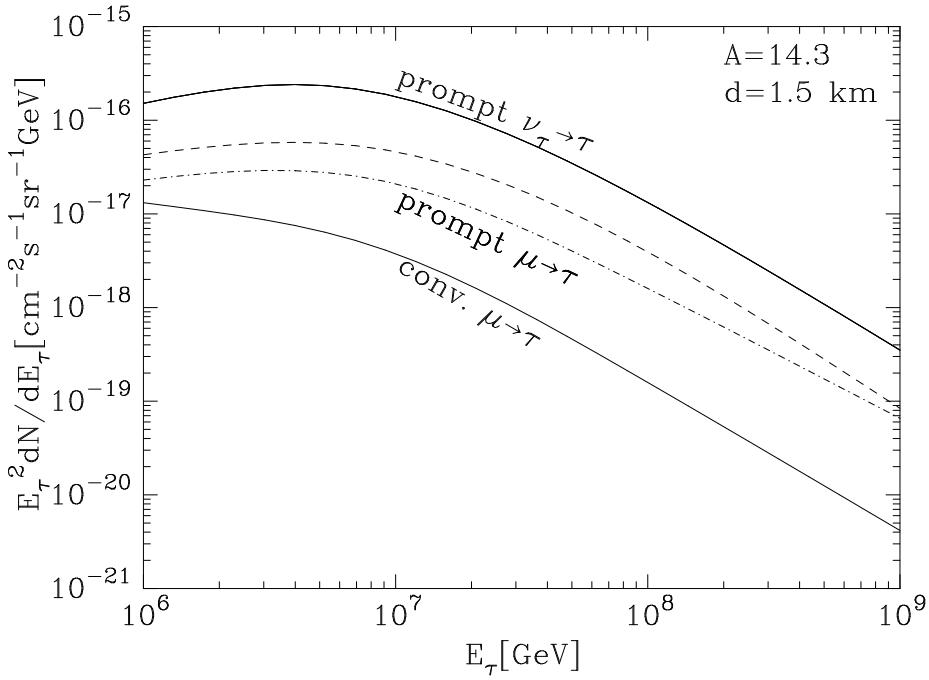

Figure 5.6: Differential tau flux scaled by the square of the final tau energy entering the detector at a depth of 1.5 km in ice. The lower solid line corresponds to tau production from a vertical incident conventional muon flux given in Eq. (4.1). The dashed and dot-dashed curve represents the tau flux from a vertical incident prompt flux given in Eq. (4.4) and Eq. (4.5) respectively. The top solid curve is for the tau flux produced with an incident prompt tau neutrino flux given in Eq. (4.8).

the detector medium. The "lollipop" event rate is proportional to $1 - P_{surv}$.

In addition to the incident fluxes that were considered in Figure 5.6, it is also instructive to look at a characteristic E_ν^{-2} dependent neutrino flux to get an idea of the relative normalization. An isotropic neutrino flux given by

$$\phi_{\nu_\tau+\bar{\nu}_\tau} = 10^{-8}(\text{cm}^2 \text{ s sr GeV})^{-1}(E/\text{GeV})^{-2} \tag{5.8}$$

gives a $\nu_\tau + \bar{\nu}_\tau$ flux that is approximately 30 times larger than the prompt $\nu_\tau + \bar{\nu}_\tau$ flux given in Eq. (4.8) that was used to calculate the underground tau flux shown in Figure 5.6 for a neutrino energy of $E_\nu = 10^5$ GeV. Because the prompt $\nu_\tau + \bar{\nu}_\tau$ flux falls approximately as E_ν^{-3}, the underground flux of taus produced from the characteristic isotropic neutrino flux given in Eq. (5.8) would remain at least a

factor of 30 higher than that produced from the atmospheric prompt tau neutrino flux given in Eq. (4.8). Therefore, if an isotropic neutrino flux with an energy dependence of E_ν^{-2} exists with the normalization of 10^{-8}, the background of tau events from the atmospheric tau neutrino flux would be very low for energies in the PeV range. It will be even more difficult to see the contribution of underground taus from incident atmospheric muons. There is the possibility that at lower energy, tau production from atmospheric leptons would be higher than that from an isotropic neutrino flux, however, the lifetime of taus at this energy is very short, making detection difficult. It is also important to note that because the differential cross section for muon induced tau production is much smaller than that for muon induced electron production, the differential flux of underground tau production shown in Figure 5.6 is much smaller than the expected differential flux of electrons shown in Figure 5.2 for the same energy regime.

5.3.2 Tau Production for HAWC

The proposed HAWC surface array has the potential to see tau decay induced showers. The array is to sit in a mountain saddle at an altitude of 4.1 km, shielded on two sides by mountains. The rock of the surrounding mountains could provide the necessary conversion volume for incident atmospheric muons and tau neutrinos and antineutrinos at high enough zenith angles to produce tau particles. Taus created in the surrounding mountains with high enough energy have the potential to exit the rock and then decay in the air above the array, producing a shower.

To investigate the potential for tau creation in the mountains shielding the HAWC array, we have assumed 1 km water equivalent distance of rock for the conversion volume. For the incident atmospheric lepton fluxes, we use a zenith angle of 45°. Figure 5.7 shows the contributions to the differential tau flux exiting the 1 km water equivalent of mountain. Shown in the figure are the contributions from

both a conventional and prompt atmospheric muon flux as well as the contribution from prompt atmospheric tau neutrinos and antineutrinos. As was the case for the underground electron fluxes, we have summed the contributions from neutrino and antineutrino production of taus and antitaus to better compare with production from atmospheric muons.

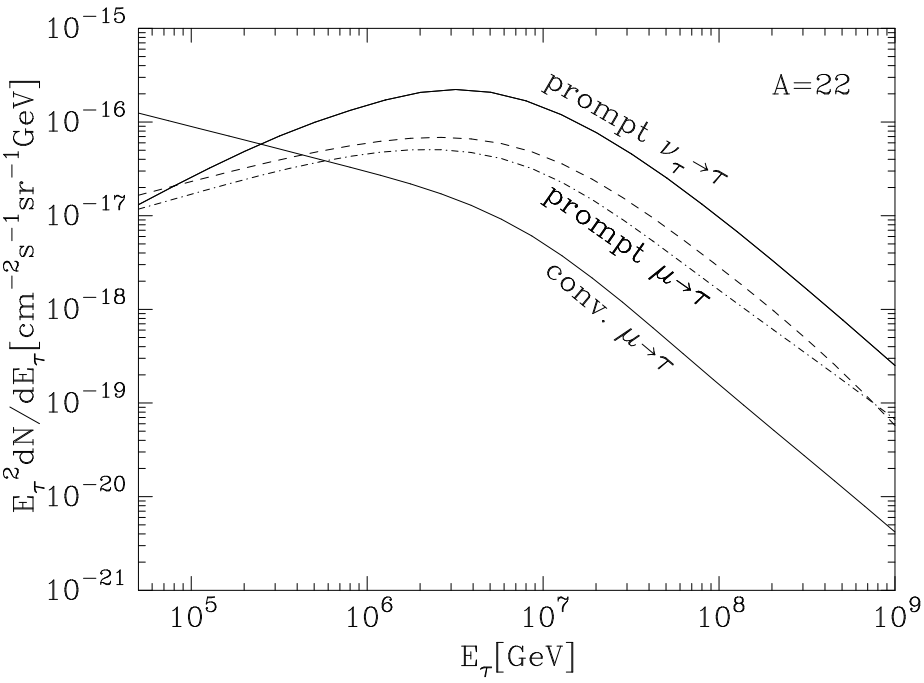

Figure 5.7: Differential tau flux scaled by the square of the final tau energy emerging from 1 km water equivalent of rock. We use a zenith angle of 45° for our incident fluxes. The lower solid line corresponds to tau production from an incident conventional muon flux given in Eq. (4.1). The dashed and dot-dashed curve represents the tau flux produced from the incident prompt muon fluxes given in Eq. (4.4) and Eq. (4.5) respectively. The top solid curve represents the tau flux produced from the incident prompt tau neutrino flux given in Eq. (4.8).

Since we are considering air showers produced by tau decays, there is no need for a minimum track length like there was in the consideration of tau particles entering IceCube. Because of this, we have lowered the lower bound of tau energy we are considering. A tau with energy $E_\tau = 10^5$ GeV has a decay length of only 5 m, so

taus exiting the mountain in this energy regime would surely decay in the air above the detector. As can be seen in Figure 5.7, the dominant contribution to the differential tau flux at this energy comes from incident conventional atmospheric muons. Due to the energy dependences of the atmospheric lepton fluxes, the contributions from conventional muons falls off much faster than the contributions from prompt muons and tau neutrinos. By $E_\tau = 10^7$ GeV, the contribution to the emerging tau flux from conventional muon conversions is suppressed by almost 2 orders of magnitude relative to the dominant prompt $\nu_\tau \to \tau$ conversion contribution. The decay length of taus with this energy is ~ 500 m which still may allow the decays to be measured by HAWC. For $E_\tau \geq 10^6$ GeV, the total differential flux of taus emerging from the 1 km water equivalent of rock receives about a $20-30\%$ contribution from atmospheric muon conversions, mostly from prompt muons.

CHAPTER 6
DISCUSSION

This calculation of the total cross section and energy loss parameter for lepton pair production in high energy μA scattering extends the work of Kel'ner [25] and others [16, 17, 18, 24, 26, 27, 28, 29, 30, 31, 32, 33, 34]. The formalism developed in Chapter 2 is valid for a large range of momentum transfers to the target nucleus. This calculation is also valid for high lepton mass as well as low.

For electron-positron pair production, where momentum transfer to the target is low, the dominant contribution to the total cross section and energy loss come from coherent scattering with the nucleus, with about a 10% contribution coming from scattering off of atomic electrons, which is scaled down by a factor of Z relative to coherent scattering. Incoherent scattering with individual nucleons and inelastic scattering effects are suppressed by $\sim 4-7$ orders of magnitude relative to coherent scattering for the muon energies considered here. A similar scaling behavior holds for calculating the energy loss parameter β_{pair} where the effects from incoherent nucleon and inelastic scattering can be neglected. Our calculation of β_{pair} for electron-positron pair production gives results that are in good agreement with those found by Kokoulin and Petrukin (KP) [18]. For muon energy $E_\mu = 100$ GeV, our calculation gives results that are $< 1\%$ lower than those found by KP. For $E_\mu = 10^8$ GeV, our calculation give results that are $\sim 4\%$ lower than KP showing the effects of nuclear screening at high energy. Our results are within the numerical accuracy of our evaluation ($< 0.1\%$) with the results found by Groom, Mokhov, and Stringanov [21] for a large range of initial muon energies.

For $\tau^+\tau^-$ pair production, we have shown that there is no simple correspondence with the simple formulas in the literature [22]. For $\tau^+\tau^-$ pair production,

larger momentum transfers need to be considered, leading to an increased contribution from incoherent nucleon and inelastic scattering effects. Coherent scattering off of the nucleus is still the dominant contribution to the total cross section and energy loss parameter for muons scattering with atomic targets for a large range of initial muon energies, however, inelastic scattering gives contributions which range from $\sim 30-60\%$ depending on initial muon energy and target. At low energies, incoherent scattering with individual nucleons gives contributions which are of the same order as those from coherent and inelastic effects. Once the threshold is reached for $\tau^+\tau^-$ production off of atomic electrons, the contributions grow quickly and are on the order of 10% for $E_\mu = 10^8$ GeV. Overall, tau pair production is not a significant source of energy loss for high energy muons in transit.

In Section 3.3.1 I have shown that the formula of Tannebaum [22] can be expressed as the differential cross section with respect to energy. With the redefinition of the fractional energy loss, $v = 2E_e/(E_\mu + \frac{1}{2}E_e)$, we can approximately reproduce our numerical calculation for the energy distribution of the differential cross section for electron-positron pair production. Using the approximate form from Tannenbaum [22] to calculate the flux of underground electrons yields errors that are $\leq 30\%$ for electron energies 10 GeV $\leq E_e \leq 10^9$ GeV. As is the case for the calculation of the total cross section and energy loss parameter, there is no easy correspondence for $\tau^+\tau^-$ pair production and we can only use our numerical evaluation for the calculation of the energy distribution of the differential cross section.

Though there are analytic formulas in the literature for the differential charged current cross section for neutrino nucleon scattering [53], they are not valid at low values of inelasticity, y, and high initial neutrino energy. They do not reflect the violation of Bjorken scaling. As the energy of the neutrino and momentum transfers increase, there is an increased contribution from sea quarks that needs to be taken

into account. I give, in Section 3.3.3, an approximate form for the charged current differential cross section for neutrino and antineutrino scattering with isoscalar nucleons. We have explicitly put energy dependence in the phenomenological parameters to account for the y dependence that is seen as the energy of the incident neutrino (antineutrino) increases. We find that the results presented here are within 15% for the y distribution of the differential cross section when compared to numerical results calculated using the CTEQ6 [54] parton distributions functions. This parameterization will be valuable for future analytic calculations requiring the charged current differential neutrino cross section. Because of the energies under consideration here, we have neglected the effects of mass of the produced lepton.

Our calculation of underground electron and photon production from incident atmospheric muons may help to augment efforts to see the onset of the atmospheric prompt muon flux. Comparing Figure 5.2 with Figure 4.2 shows that the crossover of conventional and prompt contributions to the underground electron flux produced by atmospheric muons occurs one order of magnitude lower than the crossover for conventional and prompt atmospheric muons at depth. Figure 5.3 shows that the corresponding crossover for photon events happens at an energy intermediate to these two points. Because the parameterizations of atmospheric prompt models for muon production have different crossover points [3, 5, 7, 11], the additional information provided by studying underground electromagnetic signals may help to aid in the determination of the correct prompt parameterization for the atmospheric muon flux.

Though our calculation for underground electromagnetic events has focused on production by atmospheric leptons in the vertical direction, the formalism can be generalized to higher zenith angles. The underground flux of electrons produced by conventional muons with an incident zenith angle of 30° is reduced to $\sim$ 80%

of the flux produced by conventional muons in the vertical direction between the depths of $1.5 \leq D \leq 2.5$ km for electron energy of $E_e = 10$ GeV. For the same depth, the underground electron flux produced by conventional atmospheric muons with an incident zenith angle of 30° is $\sim 90\%$ of the flux produced by atmospheric muons in the vertical direction for electron energy of $E_e = 10^9$ GeV.

While muon energy loss plays a significant role when considering the atmospheric flux at depth, neutrino attenuation is not an important feature. Due to the low cross section for neutrino nucleon scattering, the interaction length for neutrinos is on the order of 10^5 km of ice even at the highest energies [55]. Because of this, we have neglected the contributions from neutrino attenuation when considering the downward going atmospheric neutrino fluxes at depth.

When considering underground production of high energy taus, it is important to understand the signals used in underground Cherenkov detectors to identify tau events. A "lollipop" signal is identified with an electromagnetic tau track entering the detector and a splash of energy created by the tau decay, with a threshold for this type of event of ~ 5 PeV [12, 63]. While potentially difficult to see, the total tau flux considered here receives $\sim 20\%$ contribution from the prompt $\mu \to \tau$ underground flux. Conventional $\mu \to \tau$ production is not important in the energy range considered here and is suppressed by ~ 2 orders of magnitude relative to the prompt $\nu_\tau \to \tau$ signal. The "double bang" event, where there is a splash of energy left by the creation of a tau, a tau track, and another splash left by the tau decay [63], is also possible in the type of production we consider here. For tau production from atmospheric muons, the initial muon track should reduce the background from this process. While we have not done a full calculation for expected number of "double bang events", it is expected that similar to "lollipop" events, the prompt $\nu_\tau \to \tau$ flux would be difficult to see in IceCube.

The HAWC array presents another opportunity to see tau production and decay. HAWC may have the potential to see the decays of taus that are created in, and subsequently exit, the rock of the mountains surrounding the array. As I showed in Figure 5.7, for emerging tau energy of $E_\tau = 50$ TeV the dominant contribution to the tau flux comes from conventional $\mu \rightarrow \tau$ production. At this energy, all of the taus exiting the rock will decay before reaching the detector allowing for a potential detection by the surface array. For emerging tau energy of $E_\tau = 10$ PeV, corresponding to a decay length of 500 m, there is still the potential for detection of the tau decay. At this energy, prompt $\nu_\tau \rightarrow \tau$ production gives the dominant contribution to the emerging tau flux, with prompt $\mu \rightarrow \tau$ production contributing $\sim 20\%$ to the total emerging flux.

It is important to note that when considering production of high energy electron-positron pairs from muons in transit, there should be rare events where one of the charged leptons comes out with a significant fraction of the initial muon energy. In events with this type of energy distribution, it may be difficult to see the accompanying lepton, as well as the emerging muon in a large Cherenkov detector. Since even the highest energy electrons shower very quickly, this type of event creates the potential for faked "lollipop" signals when searching for tau neutrino production of underground taus. Cataclysmic muon bremsstrahlung events could produce a similar signal, adding to the potential for fake "lollipop" events. This is important because the flux of PeV electrons produced in IceCube from the vertical direction is roughly 100 times the flux of prompt tau neutrino induced tau events at a similar energy. The flux of muon bremsstrahlung events is even higher, roughly 10^4 times the prompt $\nu_\tau \rightarrow \tau$ underground flux in this energy regime.

In addition to the production of underground tau particles, there is also the potential for production of a secondary "atmospheric" tau neutrino flux coming

from incident atmospheric muons via

$$\begin{aligned} \mu A &\rightarrow \mu\tau^+\tau^- X \\ \tau &\rightarrow \nu_\tau X \ . \end{aligned} \tag{6.1}$$

As can be seen in Figure 5.7, for tau energies lower than $E_\tau \sim 200$ TeV, the dominant mechanism for underground tau production comes from conventional atmospheric muons. For these energies, taus decay very quickly, < 10 m. The decay of these low energy taus will produce a down going flux of tau neutrinos were few are expected. Because the Deep Core detector, which is to sit in the middle of the IceCube detecting volume, will lower the energy threshold to approximately 10 GeV [64], there is the potential to see $\nu_\tau \rightarrow \tau$ conversions in this lower energy regime.

Our calculation of underground lepton production has focused on Cherenkov detectors such as IceCube and HAWC, however the formulas presented in Chapter 5 are general and can be applied to many detector geometries. The Indian Neutrino Observatory (INO) presents another interesting opportunity to study underground production of charged leptons. The detecting volume of INO will consist of magnetized iron calorimeters. Looking at Figure 3.4 shows that the total cross section for electron-positron pair production increases by a factor of ~ 10 for muons scattering with iron targets relative to ice targets. This increase in the cross section will yield a higher rate of underground charged lepton production. The iron calorimeters will also be magnetized. Due to this magnetization, INO will have the capability of separating the electron (τ^-) and positron (τ^+) signals. This separation could lead to the capability of measuring the energy of the charged partner when looking at pair production events, something that could be done numerically with our calculation of the energy distribution of the differential pair production cross section.

Studying high energy lepton pair production from muons in transit offers an

opportunity to test the predictions of QED at a high energy scale. While electromagnetic interactions of muons interacting with atomic targets, particularly lepton pair production, are interesting in their own right, they also play an important role in searches for neutrino signals. Muon induced lepton signals may provide important cross checks when searching for neutrino induced lepton production. High energy lepton pair production and muon bremsstrahlung events also may augment efforts in determining correct prompt production models. This could be a valuable tool for modeling cosmic ray interactions in the atmosphere.

APPENDIX A
CHANGE OF VARIABLES AND LIMITS OF INTEGRATION

The cross section for lepton pair production by muons interacting with atomic targets involves an eight-dimensional phase-space integration. The momentum assignments are $\mu(k)+A(p) \to \mu(k_1)+\ell^+(p_+)+\ell^-(p_-)+X(p_x)$. The differential cross section found in Eq. (2.9) is written in terms of the following invariant quantities

$$\begin{aligned} Y &= -Q^2 = -(k-k_1)^2 \\ t &= -q^2 = -(p-p_x)^2 \\ \lambda_s &= S^2 - 4m_\mu^2 M_t^2 \ . \end{aligned}$$

The combination $A_{\alpha\beta}B^{\alpha\beta}_{\mu\nu}W^{\mu\nu}$ accounts for the matrix element squared of the Bethe-Heitler diagrams shown in Figure 2.1 (I). To carry out the phase-space integration, it is useful to define the following Lorentz invariant quantities following the work of Ref. [27],

$$\begin{aligned} V^2 &= \kappa^2 = (p_+ + p_-)^2 = (q+Q)^2 \\ S &= 2p\cdot k \\ X &= 2p\cdot k_1 \\ S_x &= S - X = 2p\cdot Q \\ M_x^2 &= p_x^2 \\ W^2 &= (p+Q)^2 = M_t^2 + S - X - Y \\ T &= M_t^2 - t - M_x^2 = 2p\cdot q \\ \lambda_t &= T^2 + 4M_t^2 t \\ \lambda_Y &= S_x^2 + 4M_t^2 Y \\ \Delta M^2 &= (M_x^{\min} + 2m_e)^2 - M_t^2 \ . \end{aligned}$$

In terms of the variables above, the Bjorken x variable can be written as

$$x_{\rm Bj} = \frac{q^2}{2p\cdot q} = -\frac{t}{T}$$

Using the above definitions, the phase-space integrals reduce to

$$\begin{aligned}
\mathrm{d}(PS) &= \frac{\mathrm{d}\phi_1 \mathrm{d}S_x\,\mathrm{d}Y\,\mathrm{d}V^2\,\mathrm{d}t\,\mathrm{d}M_x^2\,\mathrm{d}\phi_q}{16\sqrt{\lambda_Y\lambda_s}}\mathrm{d}\Gamma_{\rm pair} \\
\mathrm{d}\Gamma_{\rm pair} &= \delta^4(\kappa - p_+ - p_-)\frac{\mathrm{d}^3p_+}{2p_-^0}\frac{\mathrm{d}^3p_+}{2p_+^0} \\
&= \frac{1}{8}\sqrt{1-4m_e^2/V^2}\;\mathrm{d}\cos\theta_e\,\mathrm{d}\phi_e\ .
\end{aligned}$$

Using the invariants defined above, the limits of integration in the rest frame of the target are [33]

$$\begin{aligned}
(M+m_\pi)^2 &\le M_x^2 \le (\sqrt{W^2}-2\,m_e)^2 \\
4\,m_e^2 &\le V^2 \le \frac{1}{2M^2}\Big(S_xT+\sqrt{\lambda_Y}\sqrt{\lambda_t}\Big) - t - Y \\
t_{\rm min} &\le t \le t_{\rm max} \\
t_{\rm min} &= (S_x(W^2-M_x^2)+2YM_x^2-4m_e^2(S_x+2M^2)-\sqrt{U})/(2W^2) \\
t_{\rm max} &= (S_x(W^2-M_x^2)+2YM_x^2-4m_e^2(S_x+2M^2)+\sqrt{U})/(2W^2) \\
U &= \lambda_Y\big(W^4+M_x^4+16m_e^4-2(W^2(M_x^2+4m_e^2)+4m_e^2M_x^2)\big) \\
Y^{\rm min} &\le Y \le Y^{\rm max} \\
Y^{\rm min} &= \frac{\lambda_s - SS_x}{2M^2} - \frac{1}{2M^2}\sqrt{(\lambda_s-SS_x)^2-4m_\mu^2M^2S_x^2} \\
&= \frac{\lambda_s - SS_x}{2M^2} - \frac{1}{2M^2}\sqrt{\lambda_s(\lambda_s-2SS_x+S_x^2)} \\
Y^{\rm max} &= S_x - \Delta M^2 \\
S_x^{\rm min} &= \Big[\lambda_s + \Delta M^2(S+2M^2) \\
&- \sqrt{\lambda_s(\lambda_s-2S\Delta M^2+(\Delta M^2)^2-4m_\mu^2\Delta M^2)}\Big] \\
&\times (2(S+m_\mu^2+M^2))^{-1} \\
S_x^{\rm max} &= S - 2Mm_\mu\ .
\end{aligned}$$

The above limits are valid for nucleon targets. To extend to atomic targets, the

proton mass should be substituted with the appropriate target mass, $M \to M_t$. For elastic scattering, the delta function that enforces the relation $x_{\rm Bj} = 1$ can be rewritten in terms of the final hadronic state invariant mass squared, M_x^2,

$$\delta(x_{\rm Bj} - 1) = t\delta(M_x^2 - M_t^2) \ ,$$

to reduce the number of phase-space integrals.

APPENDIX B
MATRIX CONTRACTIONS

Defining the gauge invariant quantity found in Eq. (2.14) reduces the number of surviving matrix contractions, therefore simplifying the calculation. The terms f_A and f_B can found using the gauge condition $f^{\alpha\beta}Q_\beta = 0$, and can be expressed in terms of the quantities $g_{\alpha\beta}f^{\alpha\beta}$ and $p_\alpha p_\beta f^{\alpha\beta}$,

$$\begin{aligned} f_A &= \frac{1}{2}\Big(g_{\alpha\beta}f^{\alpha\beta} - \frac{4Y}{\lambda_Y}p_\alpha p_\beta f^{\alpha\beta}\Big) \\ f_B &= \frac{2Y}{\lambda_Y}\Big(-g_{\alpha\beta}f^{\alpha\beta} + \frac{12Y}{\lambda_Y}p_\alpha p_\beta f^{\alpha\beta}\Big) \ . \end{aligned}$$

Because $f^{\alpha\beta}$ is proportional to the contraction of the squared hadronic matrix element and the squared matrix element for the virtual photon contribution to the differential cross section, $\gamma^*(q) + \gamma^*(Q) \to e(p^-) + \bar{e}(p^+)$,

$$f^{\alpha\beta} \propto B^{\alpha\beta}_{\mu\nu}W^{\mu\nu} \ ,$$

the contractions $g_{\alpha\beta}f^{\alpha\beta}$ and $p_\alpha p_\beta f^{\alpha\beta}$ are given by

$$\begin{aligned} g_{\alpha\beta}f^{\alpha\beta} &= g_{\alpha\beta}B^{\alpha\beta}_{\mu\nu}g^{\mu\nu}\frac{F_1}{M} + g_{\alpha\beta}B^{\alpha\beta}_{\mu\nu}p^\mu p^\nu\frac{F_2}{(p\cdot q)M} \\ p_\alpha p_\beta f^{\alpha\beta} &= p_\alpha p_\beta B^{\alpha\beta}_{\mu\nu}g^{\mu\nu}\frac{F_1}{M} + p_\alpha p_\beta B^{\alpha\beta}_{\mu\nu}p^\mu p^\nu\frac{F_2}{(p\cdot q)M} \ . \end{aligned}$$

Where F_1 and F_2 represent the structure functions of the target. To express the above the matrix contractions it is useful to define the quantities [25]

$$\begin{aligned} D_+ &= -t - 2q\cdot p_+ \\ D_- &= -t - 2q\cdot p_- \ . \end{aligned}$$

Using the above definitions, the four surviving matrix contractions are given by

$$
\begin{aligned}
g_{\alpha\beta}B^{\alpha\beta}_{\mu\nu}g^{\mu\nu} &= 4\left(\frac{1}{D_+^2}+\frac{1}{D_-^2}\right)\Big[(q\cdot p_+)(q\cdot p_-)-2m_e^4 \\
&\quad +(p_+\cdot p_+)(\frac{t}{2}-m_e^2)+m_e^2(q\cdot p_++q\cdot p_-)+\frac{3}{2}tm_e^2\Big] \\
&\quad +8\frac{p_+\cdot p_-}{D_+D_-}\Big[p_+\cdot p_-+2m_e^2-t-q\cdot p_+-q\cdot p_-\Big]
\end{aligned}
$$

$$
\begin{aligned}
p_\alpha p_\beta B^{\alpha\beta}_{\mu\nu}g^{\mu\nu} &= 2\left(\frac{1}{D_+^2}+\frac{1}{D_-^2}\right)\Big[M^2\Big((q\cdot p_+)(q\cdot p_-) \\
&\quad +m_e^2(q\cdot p_++q\cdot p_-+t-m_e^2)\Big)+2(p\cdot p_+)(p\cdot p_-)(m_e^2-\frac{t}{2})\Big] \\
&\quad +M^2\Big(\frac{1}{D_+}-\frac{1}{D_-}\Big)^2\Big[p_+\cdot p_-(t-2m_e^2)\Big] \\
&\quad -4\Big(\frac{p\cdot p_+}{D_+D_-}-\frac{p\cdot p_-}{D_+D_-}\Big)\Big[(p\cdot p_+)(q\cdot p_-)-(p\cdot p_-)(q\cdot p_+)\Big] \\
&\quad +4\frac{p_+\cdot p_-}{D_+D_-}\Big[M^2\Big(p_+\cdot p_--q\cdot p_+-q\cdot p_-\Big)-2(p\cdot p_+)(p\cdot p_-)\Big] \\
&\quad -4(p\cdot q)\Big[\frac{p\cdot p_+}{D_-^2}(q\cdot p_-+m_e^2)+\frac{p\cdot p_-}{D_+^2}(q\cdot p_++m_e^2)\Big] \\
&\quad +4\frac{p\cdot q}{D_+D_-}\Big[(p_+\cdot p_-)(p\cdot p_++p\cdot p_-)+m_e^2(p\cdot q)\Big]
\end{aligned}
$$

$$
\begin{aligned}
g_{\alpha\beta}B^{\alpha\beta}_{\mu\nu}p_\mu p_\nu &= 4\Big(\frac{1}{D_+}+\frac{1}{D_-}\Big)\Big(\frac{p\cdot p_+}{D_+}-\frac{p\cdot p_-}{D_-}\Big)\Big[(p\cdot p_+)(q\cdot p_-) \\
&\quad -(p\cdot p_-)(q\cdot p_+)\Big]-4\Big(\frac{p\cdot p_+}{D_+}-\frac{p\cdot p_-}{D_-}\Big)^2\Big[p_+\cdot p_-+2m_e^2\Big] \\
&\quad +2\Big(\frac{1}{D_+^2}+\frac{1}{D_-^2}\Big)\Big[M^2\Big((q\cdot p_+)(q\cdot p_-)+\frac{t}{2}(p_+\cdot p_-+2m_e^2)\Big) \\
&\quad -t(p\cdot p_+)(p\cdot p_-)\Big]-2M^2t\frac{p_+\cdot p_-}{D_+D_-} \\
&\quad +4(p\cdot q)\Big(\frac{p\cdot p_+}{D_+}-\frac{p\cdot p_-}{D_-}\Big)\Big(\frac{1}{D_+}-\frac{1}{D_-}\Big)\Big[p_+\cdot p_-+2m_e^2\Big] \\
&\quad -4(p\cdot q)\Big[\frac{(p\cdot p_-)(q\cdot p_+)}{D_-^2}+\frac{(p\cdot p_+)(q\cdot p_-)}{D_+^2}-m_e^2\frac{p\cdot q}{D_+D_-}\Big]
\end{aligned}
$$

$$
\begin{aligned}
p_\alpha p_\beta B^{\alpha\beta}_{\mu\nu} p_\mu p_\nu \;=\;& 2\Big(\frac{p\cdot p_+}{D_+} - \frac{p\cdot p_-}{D_-}\Big)^2 \Big[2(p\cdot p_+)(p\cdot p_-) - M^2(p_+\cdot p_- + m_e^2)\Big] \\
& + \frac{1}{2}\Big(\frac{1}{D_+} - \frac{1}{D_-}\Big)^2 \Big[M^4\Big(2(q\cdot p_+)(q\cdot p_-) \\
& + t(p_+\cdot p_- + m_e^2)\Big) - 4(p\cdot q)\Big(M^2\Big((p\cdot p_-)(q\cdot p_+) \\
& + (p\cdot p_+)(q\cdot p_-)\Big) - 2(p\cdot p_+)(p\cdot p_-)(p\cdot q)\Big)\Big] \\
& + 2\Big(\frac{1}{D_+} - \frac{1}{D_-}\Big)\Big(\frac{p\cdot p_+}{D_+} - \frac{p\cdot p_-}{D_-}\Big)\Big[M^2\Big((p\cdot p_+)(q\cdot p_-) \\
& + (p\cdot p_-)(q\cdot p_+)\Big) + (p\cdot q)\Big(M^2(p_+\cdot p_- + m_e^2) \\
& - 4(p\cdot p_+)(p\cdot p_-)\Big)\Big] \;.
\end{aligned}
$$

These expressions are valid for e^+e^- pair production off of proton targets. For $\tau^+\tau^-$ pair production one needs to change $m_e^2 \to m_\tau^2$. To extend the calculation to higher Z targets, the proton mass, M, appearing in the above equations needs to be changed to the appropriate target mass, M_t. Using the expression for $f^{\alpha\beta}$ given in Eq. (2.14), the expression for the contraction of all of the tensors in the differential cross section reduces to

$$
A_{\alpha\beta} f^{\alpha\beta} = (4m_\mu^2 - 2Y) f_A + (S_x - M^2 Y) f_B \;.
$$

REFERENCES

[1] See, for example, E. V. Bugaev, A. Misaki, V. A. Naumov, T. S. Sinegovskaya, S. I. Sinegovsky and N. Takahashi, Phys. Rev. D **58**, 054001 (1998) [arXiv:hep-ph/9803488].

[2] S. I. Klimushin, E. V. Bugaev and I. A. Sokalski, Phys. Rev. D **64**, 014016 (2001) [arXiv:hep-ph/0012032].

[3] L. Pasquali and M. H. Reno, Phys. Rev. D **59**, 093003 (1999) [arXiv:hep-ph/9811268].

[4] A. D. Martin, M. G. Ryskin and A. M. Stasto, Acta Phys. Polon. B **34**, 3273 (2003) [arXiv:hep-ph/0302140].

[5] P. Gondolo, G. Ingelman and M. Thunman, Astropart. Phys. **5**, 309 (1996) [arXiv:hep-ph/9505417].

[6] See, e.g., P. Lipari, Astropart. Phys. **1**, 195 (1993).

[7] L. Pasquali, M. H. Reno and I. Sarcevic, Phys. Rev. D **59**, 034020 (1999) [arXiv:hep-ph/9806428].

[8] T. K. Gaisser and T. Stanev, Phys. Rev. D **57**, 1977 (1998) [arXiv:astro-ph/9708146].

[9] S. I. Dutta, Y. Huang and M. H. Reno, Phys. Rev. D **72**, 013005 (2005) [arXiv:hep-ph/0504208].

[10] A. Achterberg *et al.* [IceCube Collaboration], Phys. Rev. D **76**, 027101 (2007).

[11] R. Enberg, M. H. Reno and I. Sarcevic, Phys. Rev. D **78**, 043005 (2008) [arXiv:0806.0418 [hep-ph]].

[12] A. Silvestri [AMANDA Collaboration], Int. J. Mod. Phys. A **20**, 3096 (2005); T. DeYoung for the IceCube Collaboration, J. Phys. Conf. Ser. **136**, 022046 (2008) [arXiv:0810.4513 [astro-ph]] and references therein.

[13] P. Berghaus [for the IceCube Collaboration], Nucl. Phys. Proc. Suppl. **190**, 127 (2009) [arXiv:0812.2883 [astro-ph]] and references therein.

[14] M. Ambrosio *et al.* [MACRO Collaboration.], Phys. Rev. D **52**, 3793 (1995).

[15] M. Ageron [ANTARES collaboration], arXiv:0812.2095 [astro-ph].

[16] G. Racah, Nuovo Cim. **16**, 93 (1937).

[17] S. R. Kel'ner and Yu. D. Kotov, Sov. J. Nucl. Phys. **7**, 237 (1968).

[18] R. P. Kokoulin and A. A. Petrukhin, in Proceedings of the XII International Conference on Cosmic Rays (Hobart, Tasmania, Australia, 1971) Vol 6.

[19] W. Lohmann, R. Kopp and R. Voss, CERN Yellow Report No. EP/85-03.

[20] P. Lipari and T. Stanev, Phys. Rev. D **44**, 3543 (1991).

[21] D. E. Groom, N. V. Mokhov and S. Striganov, Atom. Data Nucl. Data Tabl. **78**, 183 (2001).

[22] M. J. Tannenbaum, Nucl. Inst. Meth. A **300**, 595 (1991).

[23] S. I. Dutta, M. H. Reno, I. Sarcevic and D. Seckel, Phys. Rev. D **63**, 094020 (2001) [arXiv:hep-ph/0012350].

[24] N. F. Mott and H. S. W. Massey, *The theory of atomic collisions*, Clarendon Press (Oxford) 1965.

[25] S. R. Kel'ner, Sov. J. Nucl. Phys. **5**, 778 (1967).

[26] Y.-S. Tsai, Rev. Mod. Phys. **46**, 815 (1974).

[27] A. A. Akhundov, D. Yu. Bardin and N. M. Shumeiko, Sov. J. Nucl. Phys. **32**, 234 (1980).

[28] S. R. Kel'ner, Phys. Atom. Nucl. **61**, 448 (1998) [Yad. Fiz. **61**, 511 (1998)].

[29] S. R. Kel'ner and D. A. Timashkov, Phys. Atom. Nucl. **64**, 1722 (2001) [Yad. Fiz. **64**, 1802 (2001)].

[30] G. R. Henry, Phys. Rev. **154**, 1534 (1967).

[31] M. J. Tannenbaum, Phys. Rev. **167**, 1308 (1968).

[32] V. Ganapathi and J. Smith, Phys. Rev. D **19**, 801 (1979).

[33] A. A. Akhundov, D. Yu. Bardin, N. D. Gagunashvili and N. M. Shumeiko, Sov. J. Nucl. Phys. **31**, 127 (1980).

[34] S. R. Kel'ner, R. P. Kokoulin and A. A. Petrukhin, Phys. Atom. Nucl. **63**, 1603 (2000) [Yad. Fiz. **63**, 1690 (2000)].

[35] Yu. M. Andreev, L. B. Bezrukov, and E. V. Bugaev, Phys. Atom. Nucl. **57**, 2066 (1994) [Yad. Fiz. **57**, 2146 (1994)].

[36] A. Bulmahn and M. H. Reno, Phys. Rev. D **79**, 053008 (2009). arXiv:0812.5008 [hep-ph].

[37] A. Bulmahn and M. H. Reno, Phys. Rev. D **81**, 053003 (2010). arXiv:0912.1385 [hep-ph].

[38] H. Abramowicz and A. Levy, hep-ph/9712415.

[39] A. Sandoval, M. M. Gonzalez and A. Carraminana [HAWC Collaboration], AIP Conf. Proc. **1085**, 854 (2009).

[40] D. Binosi and L. Theussl, Comput. Phys. Commun. **161**, 76 (2004) [arXiv:hep-ph/0309015].

[41] R. Devenish and A. Cooper-Sarkar, *Oxford, UK: Univ. Pr. (2004) 403 p*

[42] G. P. Lepage, J. Comput. Phys. **27**, 192 (1978).

[43] J. A. M. Vermaseren, arXiv:math-ph/0010025.

[44] For a review of recent results, see, e.g., C. F. Perdrisat, V. Punjabi and M. Vanderhaeghen, Prog. Part. Nucl. Phys. **59**, 694 (2007) [arXiv:hep-ph/0612014].

[45] J. J. Kelly, Phys. Rev. C **70**, 068202 (2004).

[46] Yu. M. Andreev and E. V. Bugaev, Phys. Rev. D **55**, 1233 (1997).

[47] R. Hofstadter, Ann. Rev. Nucl. Sci. **7**, 231 (1957).

[48] L. Schiff, Phys. Rev. **83**, 252 (1951).

[49] R. H. Landau and M. Mcmillan, Phys. Rev. C **8**, 2094 (1973).

[50] H. Abramowicz, E. M. Levin, A. Levy and U. Maor, Phys. Lett. B **269**, 465 (1991).

[51] A.C. Benvenuti et al. (BCDMS Collaboration), Phys. Lett. B **237**, 599 (1990).

[52] E665 Collaboration, M.R. Adams et al., Phys. Rev. Lett. **68**, 3266 (1992), Phys. Lett. B **287**, 375 (1992), Z. Phys. C **67**, 403 (1995).

[53] A. Strumia and F. Vissani, arXiv:hep-ph/0606054.

[54] J. Pumplin, D. R. Stump, J. Huston, H. L. Lai, P. M. Nadolsky and W. K. Tung, JHEP **0207**, 012 (2002) [arXiv:hep-ph/0201195].

[55] R. Gandhi, C. Quigg, M. H. Reno and I. Sarcevic, Phys. Rev. D **58**, 093009 (1998) [arXiv:hep-ph/9807264]. R. Gandhi, C. Quigg, M. H. Reno and I. Sarcevic, Astropart. Phys. **5**, 81 (1996) [arXiv:hep-ph/9512364].

[56] M. H. Reno, Nucl. Phys. Proc. Suppl. **143**, 407 (2005) [arXiv:hep-ph/0410109].

[57] S. Kretzer and M. H. Reno, Nucl. Phys. Proc. Suppl. **139**, 134 (2005) [arXiv:hep-ph/0410184].

[58] S. Kretzer and M. H. Reno, Phys. Rev. D **66**, 113007 (2002) [arXiv:hep-ph/0208187].

[59] V. Agrawal, T. K. Gaisser, P. Lipari and T. Stanev, Phys. Rev. D **53**, 1314 (1996) [arXiv:hep-ph/9509423].

[60] J. L. Feng, P. Fisher, F. Wilczek and T. M. Yu, Phys. Rev. Lett. **88**, 161102 (2002) [arXiv:hep-ph/0105067].

[61] A. A. Petrukhin and V. V. Shestakov, Can. J. Phys. **46**, S377 (1968).

[62] A. Van Ginneken, Nucl. Instrum. Meth. A **251**, 21 (1986).

[63] D. F. Cowen [IceCube Collaboration], J. Phys. Conf. Ser. **60**, 227 (2007).

[64] C. Wiebusch for the IceCube Collaboration, arXiv:0907.2263 [astro-ph.IM].